OPTICAL INTERFEROMETERS: PRINCIPLES AND APPLICATIONS IN TRANSPORT PHENOMENA

Sunil Verma [Corresponding author]
Scientist, Laser Materials Development and Devices Division, Raja Ramanna Centre for Advanced Technology, Indore 452013, India
Email: sverma1118@gmail.com, Phone: +91-731-248 8670, Fax: +91-731-248 8650

Yogesh M. Joshi
Associate Professor, Department of Chemical Engineering, Indian Institute of Technology Kanpur, Kanpur 208106, India (joshi@iitk.ac.in)

K. Muralidhar
Professor, Department of Mechanical Engineering, Indian Institute of Technology Kanpur, Kanpur 208016, India (kmurli@iitk.ac.in)

ABSTRACT

Optical techniques are extensively used for high precision diagnostics and process monitoring in physical, biological, and engineering sciences. Interferometry falls in one such class of diagnostics. It relies on changes in the refractive index in the medium arising from variations in the material density. The physical region in which imaging is being carried out is required to be transparent. The light source best suited for an interferometer is a laser. Owing to its features such as greater accuracy, resolution, instantaneous response and non-intrusive nature, interferometry proves to be advantageous and extensively utilized in broad spectrum of applications. The present chapter deals with the description of laser interferometers in visualization and monitoring of processes involving fluid flow, heat transfer, and mass transfer.

The chapter is divided into two sections. In the first section, we discuss the basic principles of interference and fringe formation. It includes the principles and operations of various interferometer configurations such as Michelson, Mach-Zehnder, holography, phase-shifting, speckle, schlieren and dual-wavelength interferometry. Interferometers can provide vivid images of temperature and solutal concentration fields. Their real utility is in the quantitative determination of transport properties in addition to heat and mass fluxes. The second section describes the applications of interferometry in studying transient heat conduction, buoyancy-driven convection in a rectangular cavity and superposed fluid layers, and crystal growth from an aqueous solution. These illustrate the utility of interferometry in engineering and research.

TABLE OF CONTENTS

1. FUNDAMENTALS

The present section is concerned with image formation when a light beam traverses a transparent medium in which density variation is present.

1.1 Optical interference

Optical methods of measurement are known to have specific advantages in terms of spanning a field-of-view and being inertia-free. In use for over half a century, optical methods have seen resurgence over the past decade. The main factors responsible are the twin developments in the availability of cost-effective lasers along with high performance computers. Laser measurements in fluid and thermal sciences have been facilitated additionally by the fact that fluid media are transparent and heat transfer applications in fluids are abundant. Whole-field laser measurements of flow and heat transfer in fluids can be carried out with a variety of configurations: shadowgraph, schlieren, interferometry, speckle and PIV, to name a few. In the present chapter, temperature field measurement in fluids by laser interferometry is addressed.

The ability to record interferograms on a PC using CCD cameras has greatly simplified image analysis. It is possible to enhance image quality and perform operations such as edge detection and fringe thinning by manipulating the numbers representing the image. Thus, image sequences can be collected and spatio-temporal data of the appropriate scalar fields can be determined.

Interferometric measurements are enabled by the following factors:

i.   Light waves that are separated by a phase difference will interfere on superposition and produce alternating bands of bright and dark fringes.

ii.   Phase difference with respect to a reference is created in a variable refractive index field.

iii.   For transparent media, refractive index has a unique relationship with the material density.

iv.   Density scales with variables such as temperature and species concentration.

Hence, spatial as well as temporal changes in temperature and concentration will generate corresponding changes in refractive index, phase and ultimately lead to fringe formation. It should be emphasized at this point that interferometry is a *differential* measurement, namely measurements of refractive index in a test section against a reference where refractive index is

Since interferometry relies on the phase of the light waves, it is evident that one should employ a light source of unique wavelength (with which the phase is associated). Thus, the light source should be monochromatic. In addition, the phase of the light waves should be stable in time for meaningful fringe patterns to form. These factors require the light source to be *coherent,* a property readily obtainable from lasers, for example, a helium-neon laser. In addition, refractive index fields create an *optical path difference* with the reference wave. Accordingly, it is required that light emerges from a *point source* and the origin for distance measurement is unambiguous. These requirements can be comfortably fulfilled when a laser is used.

Light is electromagnetic radiation with wavelengths λ falling in the visible range (400-700 nm). Light propagates in vacuum at a speed c that is independent of the wavelength. Interference effects are associated with the modulation of the electric field, magnetic field playing only a passive role. Electric field is a vector but for near parallel conditions, it is sufficient to work with its scalar form.

The principle of interference can be illustrated through a simple example. Let a wavefront move through a spatially homogeneous (reference) environment as

$$E_1 = A\sin\{\frac{2\pi}{\lambda}(ct - x)\}$$

The second wavefront moves through the test region where a physical process is in progress. Through changes in refractive index, the wave undergoes a change of phase ϕ and the electric field is obtained as

$$E_2 = A\sin\{\frac{2\pi}{\lambda}(ct - x) + \phi\}$$

Note that the second wave has the same amplitude A and wavelength λ, requiring that a single source be used for passage of light through the test and reference media.

When these two wavefronts are superimposed, the resultant electric field can be calculated as

$$E_1 + E_2 = 2A\cos\frac{\phi}{2}\{\frac{2\pi}{\lambda}(ct - x) - \frac{\phi}{2}\}$$

The amplitude of the resultant wave is

$$= 4A^2 \cos^2 \frac{\phi}{2}$$

and is perceived as a variation in light intensity. This variation is between zero and $4A^2$ in a sinusoidal form. When seen through a detector (or a camera), the image will look dark below a certain threshold and otherwise, bright. This process is the basis of fringe formation in interferometry. The superposition of two monochromatic coherence wavefronts results in addition as well as cancellation of energies and is referred to as the *interference* phenomenon.

Since one wavelength λ corresponds to a phase difference of 2π, the phase difference ϕ can be associated with a path difference δ as per

$$\delta = \frac{\lambda}{2\pi} \phi$$

The relationship between a refractive index field and the phase difference can be established as follows. Refractive index is defined as

$$n = \frac{c_0}{c}$$

where c is the speed of light in the physical region and c_0 is that in vacuum. Since $n > 1$, it is clear that the physical medium serves to slow down the electromagnetic waves. This effect is equivalent to increasing the effective distance to be traversed by the wavefronts. In this context, it is useful to define an optical path length

$$PL_1 = \int n dz$$

Here, the integration is in the *z*-direction along the passage of the light beam. In general, this integration is to be performed along the path of the light ray. Further, in vacuum, $n=1$ and the path length is simply the geometric length of the apparatus in the viewing direction. In other contexts, the effective distance to be covered by the light wave (referred to its speed in vacuum) is greater by a factor that depends on the refractive index.

The reference wave passes through a region of constant refractive index leading to an optical path length

$$PL_2 = \int n_0 \ dz$$

On superposition, the path length difference is obtained as

$$\Delta PL = PL_1 - PL_2 = \int (n - n_0) \ dz$$

The equivalent phase difference is calculated from the equation

$$\Delta PL = \frac{\lambda}{2\pi}\phi$$

In a refractive index field, n would vary from one point to another. Accordingly, the path length difference and hence the phase field will be a spatial variable. Lines of constant phase (specifically those that minimize and maximize intensity) will appear as fringes. These would also be lines of constant refractive index of the material in the test section, material density, and ultimately, lines of constant temperature and solute concentration.

The path length calculation is simplified if the refractive index field is two dimensional (independent of the z-coordinate). For a domain of length L in the direction of propagation of light

$$\Delta PL = PL_1 - PL_2 = \int (n - n_0)\ d\ z \approx (n - n_0)L$$

The corresponding phase difference is

$$\phi = \frac{2\pi}{\lambda}(n - n_0)L$$

Interferograms contain information on the phase field. The above formula enables a conversion of the phase information to refractive index. It is now important to comment on the relationship between refractive index and material density of the region being investigated. The relationship is unique and is given by the Lorenz-Lorentz formula [Kumar, 2008]

$$\frac{n^2 - 1}{\rho(n^2 + 2)} = \text{constant}$$

For gases, $n \sim 1$ and the generalized relationship reduces to the Gladstone-Dale formula

$$\frac{n - 1}{\rho} = \text{constant}$$

The sensitivity of the measurement depends on the derivative $dn/d\rho$, small values of the derivative generating a smaller number of fringes in the image plane. The density–temperature/ concentration relationship is material-specific and can be obtained from an *equation of state*. Typical values of dn/dT are

air, 0.927×10^{-6} K^{-1}

water, 0.88×10^{-4} K^{-1}

It is clear that the number of fringes in water, as a rule, would be considerably larger when compared to air.

The rest of the chapter is concerned with specific optical configurations for the generation of fringe patterns and selected applications.

1.2 Why use optical techniques for imaging transport phenomena?

One could measure fluid properties with external transducers. However, in order to get sufficient data one has to deploy a large number of such probes, which start interfering with the process under study. On the other hand, only a few probes provide inadequate data. For example, a single moving probe in a liquid medium yields temporally inaccurate data if moved slowly, but stirs the system if moved rapidly. Therefore, external probes are never a satisfactory method for spatially mapping a physical domain. In contrast, optical techniques are *photon probes* that do not affect the process being studied. They map the properties of the process with a spatial resolution of about a micrometer and a temporal resolution of about a millisecond. Their response is practically inertia-free and provides a large volume of data of the process under study. Further, the availability of high speed cameras for image acquisition and powerful computers for data reduction have helped in revival of optical diagnostics in engineering research in the last decade.

1.3 Optical imaging techniques

Various types of optical imaging techniques have been used for studying transport behavior of momentum (fluid mechanics), thermal energy (heat transfer) and transport of molecular species (mass transfer). Overall, these optical techniques can be subdivided into three categories. In the first category flow marking is carried out by using dyes, bubbles, buoyant seeds, etc. in order to enable direct visualization of the fluid motion. In the second class of techniques fluid motion is studied by analyzing the frequency of an incident radiation, which is known to undergo Doppler-shift after getting scattered from the particles moving with the flow (e.g. laser Doppler velocimetry). The third category considers all those techniques which analyze behavior of an index of refraction of the medium through which the light beam propagates due to various impetuses such as fluid motion, temperature gradient and/or concentration changes (e.g. shadowgraphy, schlieren, interferometry, etc.). In this chapter we will focus only on the third of techniques.

The techniques based on alteration of refractive index n take advantage of unique relation between n and the density of the medium ρ for transparent mediums. Since transported variables such as heat (temperature) or mass of chemical component (concentration) directly affects the density, monitoring of refractive index n directly gives an information about temperature or concentration gradients in the medium. Although various techniques mentioned in the third category require variation in refractive index in order to analyze transport behavior, they have complimentary characteristics. Usually, interferometry is used when the expected changes in the refractive index are small, whereas shadowgraphy and schlieren are used when the changes in the refractive index are large. Non-interferometric techniques such as shadowgraph or schlieren rely on detection of path of light rays as they traverse through the region of interest. On the other hand interferometric methods detect optical path-length differences. Principally, the three techniques measure the physical property in an integrated manner, such that the image output is an integration of the physical quantity of interest along the path of the beam through the process chamber. Therefore, these methods show the best results when the transport is two-dimensional and light passes perpendicular to this two dimensional plane. Usually these techniques are employed when the field is nearly two dimensional, i.e. when variation of a physical quantity under investigation is negligible in the third dimension. However, if this assumption is not valid, then variation in the third dimension needs to be obtained by applying analytical techniques such as computerized tomography. The non-interferometric techniques are simpler to implement and difficult to interpret quantitatively, while the interferometric techniques are amenable to quantitative analysis though difficult to set up and maintain.

The application of interferometry are discussed in the context of monitoring the following transport processes: transient heat conduction, solutal transport, buoyancy-driven convection in a rectangular cavity, buoyancy-driven convection in superposed fluid layers, and growth of a crystal from its aqueous solution.

1.4 Imaging fluid flow

Fluid motion and convection phenomena can be visualized by optical techniques through either (a) refractive index in the form of optical path difference (or its gradient), (b) displacement of fluid markers as a function of time, or (c) velocities of fluid markers. *Flow Visualization* by Merzkirch [Merzkirch, 1987] is a classical text for researchers planning to conduct fluid flow

and convection imaging. Similarly, text books on *Optical Interferometry* by Steel [Steel, 1983] and Hariharan [Hariharan, 1985] are a good starting point for familiarizing oneself with the subject. A survey of holographic interferometry is given by Vest in his book [Vest, 1979]. *Optical Measurements: Techniques and Applications*, edited by Mayinger [Mayinger, 1994] and *Schlieren and Shadowgraph Techniques*, by Settles [Settles, 2001] present excellent compendia of a variety of optical techniques for fluid flow and convection mapping.

1.4.1 Shadowgraph

Shadowgraphy employs a collimated beam of light from either a white light source or a laser. The image has uniform contrast if there are no refractive index gradients in the region of interest. On the other hand, due to the curvature of light rays by the refractive index gradients, the portions of the image corresponding to the displaced rays appear bright or dark. Shadowgraph systems are simple and have been extensively used in experimental fluid mechanics research for flow visualization [Goldstein, 1996; Settles, 2001]. Figure 1 shows the schematic drawing of a shadowgraph optical set up and the image acquisition system.

Under the assumption of infinitesimal deviation of light rays inside the inhomogeneous field and also between the exit face of the process chamber and the screen, the linear governing equation for the shadowgraph process is [Schopf, 1996; Verma, 2005]:

$$\frac{I_o(x_i, y_i) - I_s(x_s, y_s)}{I_s(x_s, y_s)} = \left(L \times D\right)\left(\frac{\partial^2}{\partial x^2} + \frac{\partial^2}{\partial y^2}\right)\{\ln n(x, y)\}$$

Here I_0 is the intensity at a particular point (x_i, y_i) on the screen in the absence of the field of disturbance; I_s is the intensity at point (x_s, y_s) due to intensities $I_0(x_i, y_i)$ of all the points (x_i, y_i) which are mapped onto (x_s, y_s) in the presence of the field of disturbance; D is the spread of the field of disturbance; L is the distance between the exit surface and the screen; and $n(x, y)$ is refractive index at the location (x, y).

1.4.2 Schlieren

Schlieren technique requires a collimated light system and converging lens with a knife-edge that is introduced halfway into the focal point [Goldstein, 1996; Settles, 2001]. Light rays deflected (by refractive index gradients) toward the knife edge are blocked resulting in dark spots on the

image; conversely, rays deflected away from the knife edge show as bright spots on the screen. The knife-edge can be oriented either vertically or horizontally, thus enabling measurement of refractive index gradients in the two directions. The governing equation for the schlieren process under the linear approximation is

$$\frac{I_o - I_s}{I_s} = \frac{2f}{a}\left(\frac{\partial}{\partial y}\{\ln n(x, y)\}\right)$$

where a is the source size and f is the focal length of the lens used for focusing the beam over the knife-edge. As is evident from the above equation, a single integration is needed to extract the refractive index field from the schlieren image as compared to double integration required in case of solving a Poisson equation for shadowgraph image.
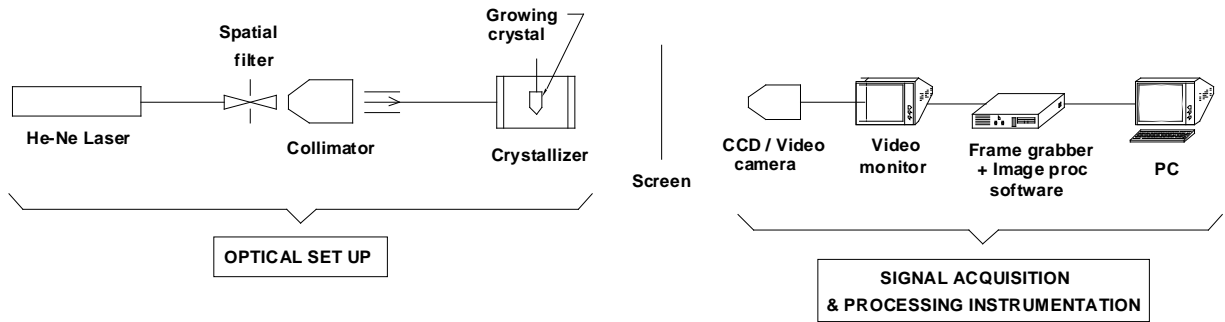
Figure 1: Schematic drawing of a shadowgraph optical set up and the image acquisition instrumentation
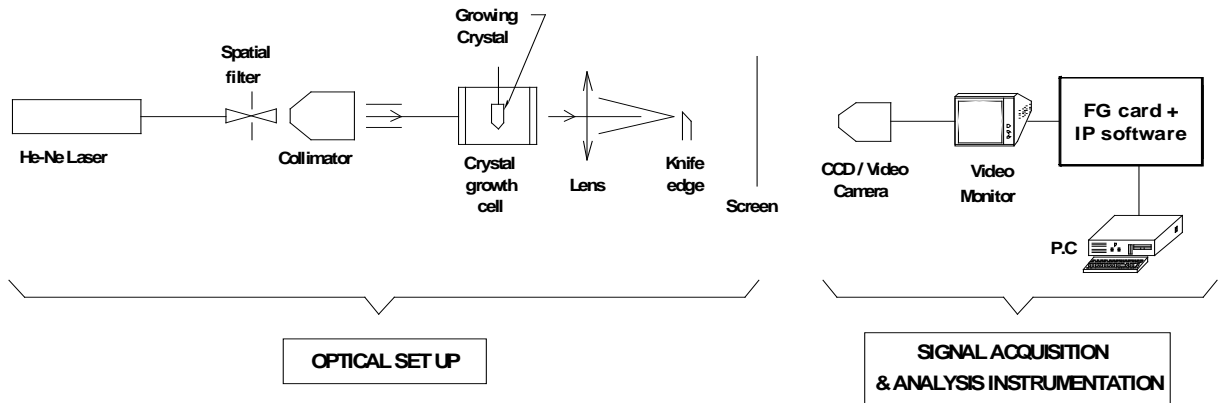
Figure 2: Schematic drawing of a schlieren optical technique

1.4.3 Interferometric methods

The physics behind the generation of interferograms is different from shadowgraph and schlieren techniques. In interferometry, the phase change of the test beam with respect to the reference beam is the origin of the formation of interferograms. As a rule, interferometry is used when the expected changes in temperature or concentration are small. If the thermal or solutal changes in the region of interest are large, they limit the usefulness of interferometry in process monitoring for the following reasons: (i) the linearity between density (through temperature or concentration) and refractive index breaks down; and (ii) large gradients in the temperature and concentration fields result in sharp bending of rays. Both these effects complicate interferometric data analysis.

1.4.3.1 Schlieren-Interferometer

This technique has the characteristics of both non-interferometric and interferometric methods in that it detects the curvature as well as the path length of the light rays. Since the final experimental output is an interference pattern, we have classified it as an interferometric technique. It is also referred to either as a *Wollaston-prism shearing interferometer* or a *differential interferometer* [Mayinger, 1994, pp. 78-83; Settles, 2001, pp. 132-134]. The Wollaston prism uses double refraction to separate an incident light ray into two rays which are polarized orthogonally to each other and diverge from each other at an angle of $\pm\theta/2$ with respect to the original direction of the beam (Figure 3). Collimated monochromatic light is passed through a polarizer, set at an angle of 45° to the direction of separation of the Wollaston prism, so as to produce e- and o- rays of equal intensity on passing through the prism. The parallel-ray polarized beam then passes through the solution in the test cell and is then focused by a lens into the Wollaston prism. As the polarized rays traverse through this prism, they split into e- and o-rays. Incident ray 1 is separated into two rays 1_e and 1_o, representing polarization parallel and perpendicular to the plane of the diagram. On leaving the prism, these two rays have an angle of θ between them. Adjacent incident rays 2, 3… are similarly split, as shown. Since the rays 1 and 2 have a separation of θ between them, ray 1_e coincides with 2_o, and similar pairings occur for all adjacent rays having separation of θ, i.e. the ray 2_e coincides with 3_o, and so on. Since the coinciding rays have orthogonal planes of polarization, there is no interference between them. But when passed through a polarizer oriented at 45° to the separation direction of the Wollaston

prism, the emerging paired wavefronts interfere and an interference pattern is obtained on the screen. In short, the collimated image from the experimental test cell is split by the Wollaston prism into two mutually displaced images which then interfere with each other. Therefore each element of the final image represents the interference between P_{xy} and $P_{x(y+k)}$, where P is the optical path length at image coordinates x and y. If the prism is centered upon the focus of the converging lens, infinite-fringe mode interference results, which resembles a schlieren image. Displacement of the centre of the Wollaston prism from the focal point results in wedge fringes to appear in the image. The bends in the wedge fringes are proportional to the refractive index gradients in the test region and can be used for quantitative evaluation. The principal virtue of the schlieren interferometer is the flexibility of being able record quasi-schlieren images, which facilitate qualitative interpretation, to multiple-fringe images for quantitative measurements.
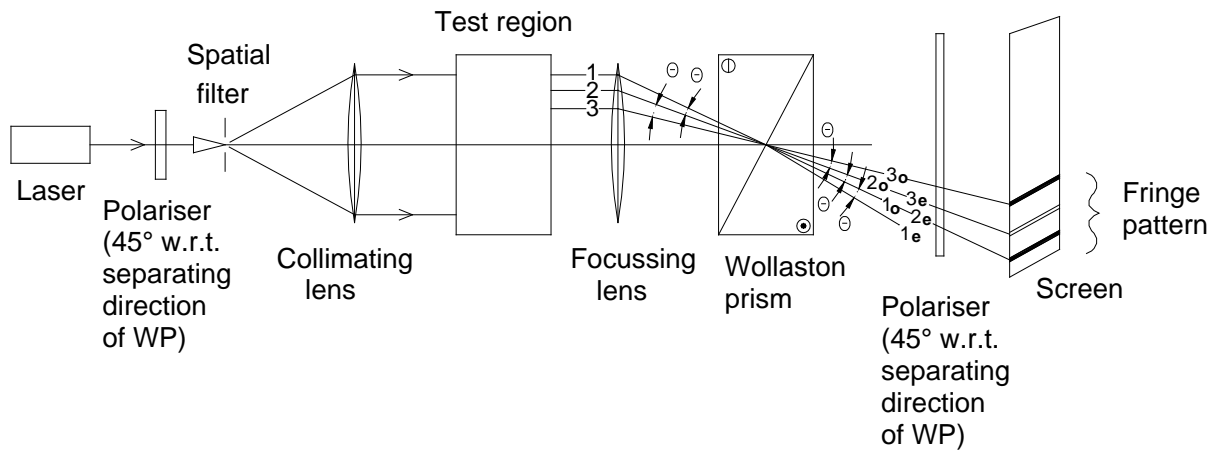
Figure 3: Optical layout of a schlieren (differential) interferometer [Verma, 2008].

1.4.3.2 Mach-Zehnder interferometer

The Mach-Zehnder interferometer is a popular configuration for studies in heat and mass transfer in fluids. The optical components namely beam splitters and mirrors are inclined exactly at an angle of 45° with respect to the beam direction (Figure 4). The first beam splitter splits the incoming collimated beam into two equal parts, namely the transmitted and reflected beams. The transmitted beam is the *test beam* and the reflected beam is the *reference beam*. The test beam passes through the test region, is reflected by the mirror, and recombines with the reference beam on the plane of the second beam splitter. The reference beam undergoes a reflection at the second

mirror and passes through the reference medium and superposes with the test beam at the second beam splitter. On superposition, the two beams produce an interference pattern. This pattern contains information about the variation of refractive index in the test region.

The Mach-Zehnder interferometer can be operated in two modes, namely infinite fringe setting and wedge fringe setting (Figures 5(a-d)). In the former the test and reference beams are set to have identical geometrical path lengths, and the fringes form due to refractive index changes alone. Since each line is a line of constant phase, it is also a line of constant refractive index. The fringe thickness is an inverse measure of the local refractive index gradient, being smaller when the gradients are high. This setting is used for high-accuracy refractive index measurements. In the wedge fringe setting, the mirrors and beam splitters are deliberately misaligned to produce an initial fringe pattern of straight lines. When a refractive-index disturbance is introduced in the path of the test beam, these lines deform and represent refractive index profiles in the fluid. The quantitative methodology of extracting temperature change per fringe shift from the wedge and infinite settings is described below.
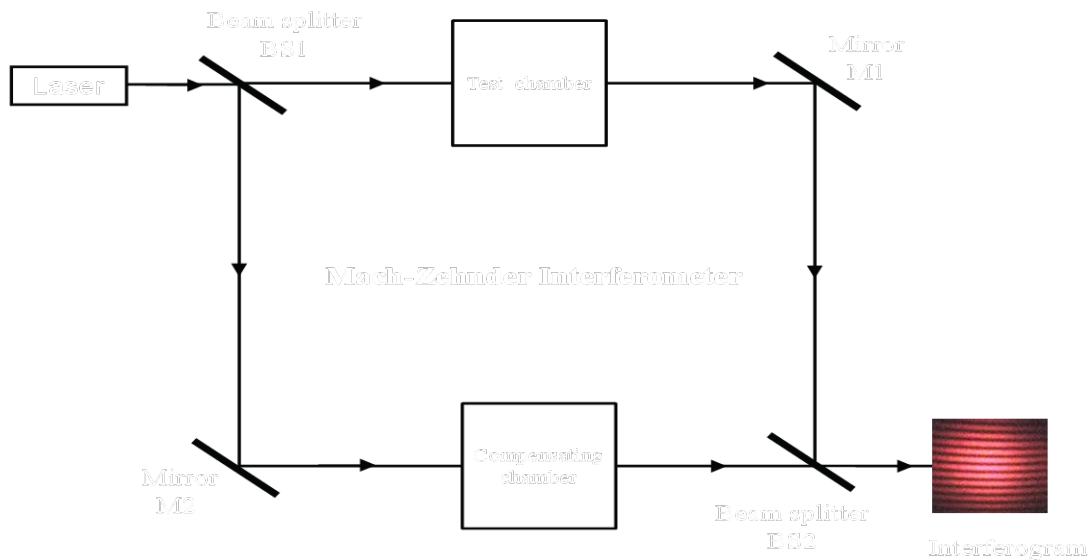

Figure 4: Optical configuration of a Mach-Zehnder interferometer. A compensation chamber may be required in the path of the reference beam to cancel effects arising from an undisturbed medium in the test cell.
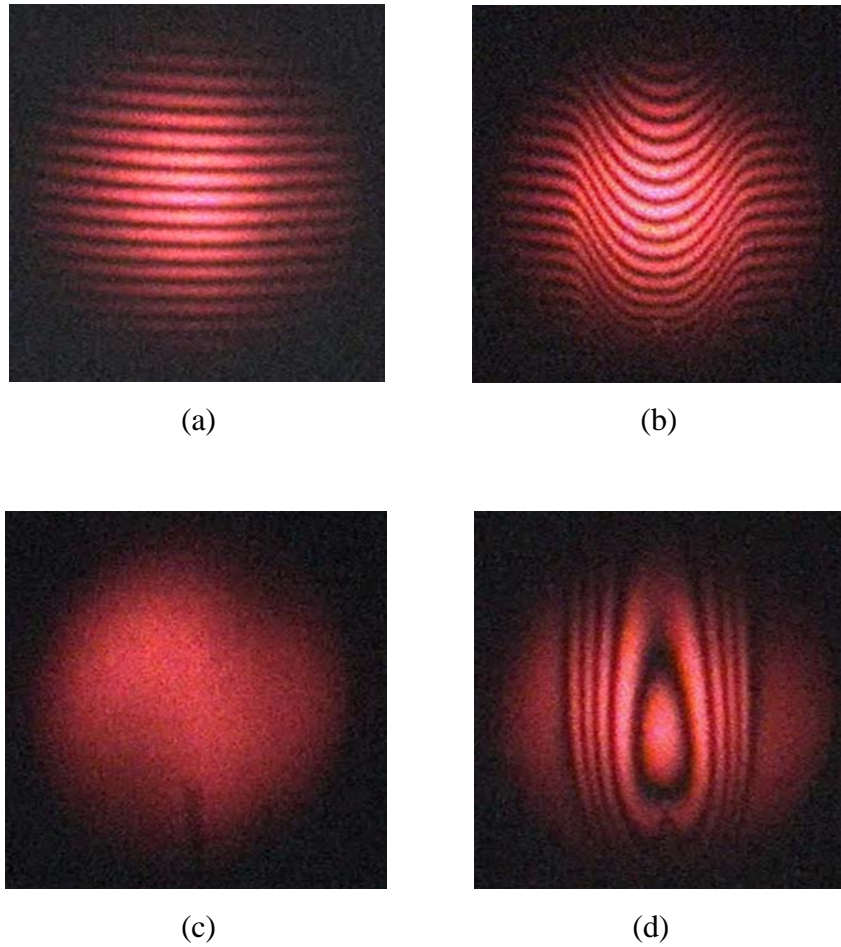
Figure 5: Mach-Zehnder interferograms. (a) Wedge fringes, (b) Candle flame in the wedge fringes, (c) Infinite fringe, and (d) Candle flame in the infinite fringe

Let $n(x,y,z)$ and $C(x,y,z)$ be the refractive index and concentration fields respectively in the physical domain of interest. With reference to the test chamber, coordinates x and y form the vertical plane, which is perpendicular to the beam propagation direction, and the z-axis is the horizontal line along the length of the test section. The light beam propagates parallel to the z-axis. Let n_o and C_o be the reference values, as encountered by the reference beam passing through a compensating chamber. The interferogram is a fringe pattern arising from the optical path difference

$$\Delta PL(x, y, z) = \int_0^S \left[n(x, y, z) - n_o \right] d\,z$$

which in terms of concentration is

$$\Delta PL(x, y, z) = \frac{dn}{dC} \int_0^S \left[C(x, y, z) - C_o \right] d_{\,\scriptscriptstyle s}$$

The above integral is evaluated along the path of the light ray given by the coordinate *s*. If we neglect higher order optical effects such as refraction and scattering, the path of the light ray will be straight along the length of the test chamber. Since the interference fringes are loci of constant phase or constant phase difference, the optical path difference ΔPL is constant on a given fringe. Therefore

$$\int_0^L \left[C(x, y, z) - C_o \right] dz = \frac{\Delta PL(x, y, z)}{dn/dC} = \text{constant}$$

and it follows that

$$\int_0^L C(x, y, z) dz \ - \ C_o L = \text{constant}$$

for a given fringe.

The integral $\int_0^L C(x, y, z) dz$ is equal to $\overline{C}L$, where $\overline{C}$ is the average value of the variable $C(x,y,z)$ along the length *L* traversed by the laser beam inside the test chamber. Under the approximation of negligible refraction, the above integral reduces to a line integral of the function $C(x,y,z)$ along the *z*-axis. Hence, we get

$$(\overline{C} - C_o)\, L = \text{constant} = \frac{\Delta PL}{dn/dC} \qquad (1)$$

This equation holds for all the fringes in the case of the infinite-fringe setting. Each fringe of the interferogram represents a locus of points over which the average of the concentration field evaluated along the length of the test chamber is constant; i.e. the fringes are isoconcentration contours. In processes governed predominantly by thermal changes, fringes correspond to isotherms. For a change in path length by one wavelength, one fringe shift occurs. Since this change in path length per fringe shift is constant, the change in concentration per fringe shift is also a constant. Defining the function $(\overline{C} - C_o)\, L$ in Equation (1) as $f(\overline{C}, L)$, the concentration at two successive fringes for a given value of *L* can be obtained as

$$\text{fringe 1:} \qquad f_1(\overline{C_1}, L) = \frac{\Delta PL}{dn/dC}$$

fringe 2: $$f_2(\overline{C_2}, L) = \frac{(\lambda + \Delta PL)}{dn/dC}$$

where λ is the wavelength of the laser. From these two equations the concentration change per fringe shift can be calculated as

$$\Delta C_E = \frac{1}{L}\left\{f_2(\overline{C_2}, L) - f_1(\overline{C_1}, L)\right\} = \frac{\lambda/L}{dn/dC} \qquad (2)$$

The number of fringes expected in a projection can be estimated from the relation

$$\text{Number of fringes } = \frac{C_2 - C_1}{\Delta C_E}$$

This relation is valid when (a) the refraction effects are negligible and (b) the test beam is traversing through a single fluid.

Now consider the situation wherein concentration gradients are large and the ray traverses a different distance through the cell. Let the two light rays traverse paths L_1 and L_2 respectively inside the test cell, and the corresponding line integrals of the concentration field $C(x,y,z)$ resulting in the average concentrations be $\overline{C_1}$ and $\overline{C_2}$ respectively. Using Equation (1) we can write

$$(\overline{C_2} - C_o)\, L_2 = (\overline{C_1} - C_o)\, L_1\,.$$

Thus, the line integral value $\overline{C_2}$ at a location on the fringe which corresponds to the length L_2 can be expressed in terms of the line integral value $\overline{C_1}$ at some other location corresponding to the ray length L_1 as

$$\overline{C_2} = C_o + \frac{L_1}{L_2}\left(\overline{C_1} - C_o\right).$$

1.4.3.3 Refraction effects

The presence of strongly refracting fields can modify Equation (2) for the concentration difference per fringe shift. In the present context, a strongly refracting field will arise when there is large concentration or thermal difference in the vertical direction inside the test cell. Hence, the light ray will not travel in a horizontal plane; instead it will bend in the vertical direction, the extent of which depends on the magnitude of the concentration or thermal gradient. Therefore refraction will introduce an additional path length for the test beam. For the sake of completeness of the discussion on interferometric imaging, we present below the derivation of the formula for

calculating the change in concentration per fringe shift under the presence of strongly refracting fields.

Consider the path of the light ray AB through a test cell (Figure 6) when it is affected by refraction effects. Let α be the bending angle at a location P of the test cell. The optical path length from A to B is given by

$$AB = \int_A^B n(x, y, z) \, ds$$

$$= \int_0^L n(x, y, z) \, \frac{dz}{\cos \alpha}.$$

Here y is a coordinate parallel to the gravity vector and z is parallel to the direction of propagation of light. The length of the test section in the z-direction is indicated as L.

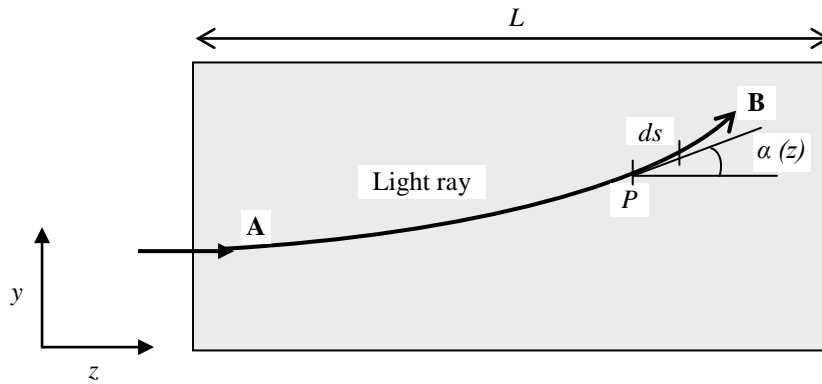Figure 6: Bending of the light ray due to refraction effects.

Assuming α to be small, $\cos(\alpha)$ can be expressed as

$$\cos \alpha = (1 - \alpha^2)^{1/2}.$$

Using the first two terms of the binomial expansion, one can approximate

$$\cos \alpha \sim 1 - \frac{\alpha^2}{2}$$

Hence the optical path length is given by

$$AB = \int_0^L n(x, y, z) \left(1 - \frac{\alpha^2}{2}\right)^{-1} dz$$

$$= \int_0^L n(x, y, z) \left(1 + \frac{\alpha^2}{2}\right) dz \qquad (3)$$

The cumulative bending angle $\alpha(z)$ at any location along the z axis can be easily calculated. It can be shown that the expression for the bending angle $\alpha(z)$ is (Goldstein, 1996)

$$\alpha(z) = \frac{1}{\overline{n}(x, y)} \frac{\partial \overline{n}(x, y)}{\partial y} z \qquad (4)$$

where $\overline{n}(x, y)$ is the average line integral of $n(x, y)$ over the test cell dimension L. Similarly the expression $\partial \overline{n}(x, y)/\partial y$ represents the average line integral of the transverse derivative of $n(x, y)$ over the length L.

Substituting the expression for $\alpha(z)$ from Equation (4) in Equation (3) we get

$$AB = \int_0^L n(x, y, z) \left[1 + \frac{1}{2} \frac{1}{\overline{n}^2} \left(\frac{\partial \overline{n}}{\partial y}\right)^2 z^2\right] dz$$

$$= \overline{n}(x, y) L + \frac{1}{6 \overline{n}} \left(\frac{\partial \overline{n}}{\partial y}\right)^2 L^3$$

The optical path of the reference beam is

$$AB = \int_0^L n_o dz$$

$$= n_o L$$

Hence the difference in the optical path lengths of the test and reference beams in the presence of refraction effects is

$$\Delta PL = \overline{n}(x, y) L + \frac{1}{6 \overline{n}} \left(\frac{\partial \overline{n}}{\partial y}\right)^2 L^3 - n_o L$$

$$= \left(\overline{n}(x, y) - n_o\right) L + \frac{1}{6 \overline{n}} \left(\frac{\partial \overline{n}}{\partial y}\right)^2 L^3$$

$$= \left(\overline{C_1}(x, y) - C_o\right) L \frac{dn}{dC} + \frac{1}{6 \overline{n}} \left(\frac{\partial \overline{n}}{\partial y}\right)^2 L^3$$

where $\overline{C}_1(x, y)$ represents the average line integral of the temperature field along the direction of the ray at a given point on the fringe. The corresponding ray over the next fringe corresponds to an additional path of λ and can be written as

$$\Delta PL + \lambda = \left(\overline{C}_2(x, y) - C_o\right)L\frac{dn}{dC} + \frac{1}{6\,\overline{n}}\left(\frac{\partial \overline{n}}{\partial y}\right)^2 L^3$$

where $\overline{C}_2(x, y)$ represents the average line integral of the temperature field along the direction of the ray at a point on the next fringe. The successive temperature difference between the two fringes is

$$\lambda = \left(\overline{C}_2(x, y) - \overline{C}_1(x, y)\right)L\frac{dn}{dC} + \frac{1}{6\,\overline{n}}\left(\frac{d\overline{n}}{dC}\right)^2\left(\left(\frac{\partial C}{\partial y}\Big|_2\right)^2 - \left(\frac{\partial C}{\partial y}\Big|_1\right)^2\right)L^3$$

and the concentration change per fringe shift is

$$\Delta C_E = \frac{\lambda - \left(\frac{1}{6\overline{n}(x, y)}\right)\left(\frac{d\overline{n}}{dC}\right)^2\left(\left(\frac{\partial C}{\partial y}\Big|_2\right)^2 - \left(\frac{\partial C}{\partial y}\Big|_1\right)^2\right)L^3}{L\left(\frac{dn}{dC}\right)}.$$

Since the gradient in the concentration field is not known before the calculation of the fringe concentration, the factor $\left(\frac{\partial C}{\partial y}\Big|_2\right)^2 - \left(\frac{\partial C}{\partial y}\Big|_1\right)^2$ must be calculated from a guessed concentration field. Thus the final calculation of ΔC_E relies on a series of iterative steps with improved estimates of the concentration gradients.

1.4.3.4 Evaluation of interferograms

The thinned fringes carry the essential information of the process parameter rather than the thick fringe bands. Hence, in order to extract quantitative data from the Mach-Zehnder interferograms, we have to obtain the fringe skeleton. For our process, the thinned fringes contain the information about the path-integrated concentration field. In the sub-sections below we discuss the methodology for calculating the concentration field from interferograms recorded in the infinite- and wedge-fringe settings.

1.4.3.5 Infinite fringe interferograms

Let us consider an infinite fringe interferogram as shown in Figure 7. The presentation is in the context of a concentration field (of salt in water, for example) that varies from C_{sat} to $C_{supersat}$. The reference is to a crystal growth process discussed latter in this chapter. The aim of the following discussion is to find the absolute concentration corresponding to each fringe curve. We know that the change in concentration per fringe shift is given by

$$\Delta C_E = \frac{\lambda/L}{dn/dC}$$

and

$$C_2 - C_1 = \frac{\lambda/L}{dn/dC}$$

At the top boundary the concentration is known to be the saturation concentration C_{sat}, whereas the bottom is at a concentration equal to the supersaturation value $C_{supersat}$. Our aim is to find the concentrations C_1, C_2 and C_3 at the fringes 1, 2 and 3 respectively in the interferogram (Figure 7) with the given boundary conditions. Although the concentration values at the lower and the upper boundaries are known, assigning concentration to the first fringe appearing near the boundary is not straightforward. This is because the concentration gradients near the boundary result in several fine fringes that are lost because of the finite resolution of the CCD/video camera. Also, the first fringe may be distorted during the image processing operations. Hence it becomes necessary to assign concentration to the first visible fringe by an appropriate analytical procedure. The methodology of finding the concentration values at the first and the subsequent fringes is presented below.

Step-1: First identify that region of the interferogram where the fringes are closely packed. The fringes 1, 2, and 3 are three such fringes in the above interferogram (Figure 7).

Step-2: Fitting a second-order polynomial of the type $C(y) = \alpha + \beta y + \gamma y^2$ to the three fringes, we get

$$C_1 = \alpha + \beta y_1 + \gamma y_1^2$$

$$C_2 = \alpha + \beta y_2 + \gamma y_2^2$$

$$C_3 = \alpha + \beta y_3 + \gamma y_3^2$$

where y is the vertical coordinate measured from the lower boundary. An exploded view of the three fringes and the coordinate axis is shown in Figure 8. Using above equations we obtain two simultaneous equations for the two unknowns β and γ:

$$\Delta C_E = C_1 - C_2 = \beta (y_1 - y_2) + \gamma (y_1^2 - y_2^2)$$

$$\Delta C_E = C_2 - C_3 = \beta (y_2 - y_3) + \gamma (y_2^2 - y_3^2)$$

These are solved to obtain the constants β and γ. Here, ΔC_E is the concentration change per fringe shift in the fluid.

Step-3: The next step in the analysis procedure is to compute the concentration gradient near the boundary close to the fringes. In the interferogram shown in Figure 9, we are interested in finding the concentration near to the lower boundary.

The concentration gradient at the boundary can be given as

$$\left. \frac{\partial C}{\partial y} \right|_{y=y_o} = \beta + 2 \gamma y_o \ .$$

Step-4: Once the concentration and the concentration gradient at the boundary are known, the concentration at fringe 1 near the lower boundary can be obtained as

$$C_1 = C_{boundary} + \left. \frac{\partial C}{\partial y} \right|_{boundary} (y_1 - y_o)$$

and so

$$C_1 = C_{\text{supersat}} + (\beta + 2 \gamma y_1)(y_1 - y_o)$$

Step-5: ΔC_E is the quantum of concentration change per fringe shift; thus concentration at subsequent fringes 2, 3 and others can be computed by adding it to the concentration of the previous fringe. However, if the concentration gradient is negative in the counting direction, an equivalent amount has to be subtracted.

Step-6: Since the interferogram is digitized and stored in a computer in the form of a matrix of integers, the above procedure of computing concentration can be implemented for any element of the matrix. In our experiment the concentration is a smoothly varying function, and it is expected that the concentration difference between adjacent rows of the matrix will be small. Hence the evaluation procedure is applied to the rows coinciding with the fringe locations but not in the gap between them.
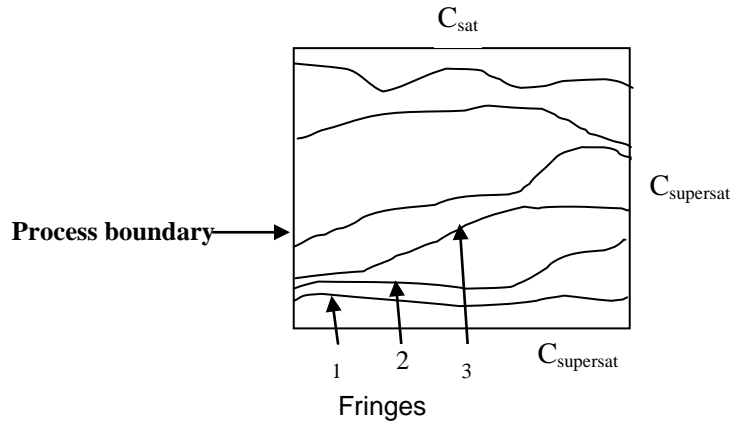
C_{sat}

Process boundary →

$C_{supersat}$

1 2 3

$C_{supersat}$

Fringes

Figure 7: Infinite fringe interferogram of the concentration field in an experiment that develops a concentration distribution.
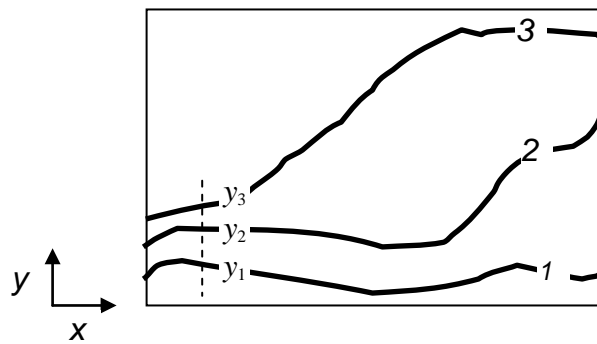

3

2

y_3

y_2

y_1

1

y

x

Figure 8: An exploded view of the fringes 1, 2 and 3 along with the coordinate system used.

1.4.3.6 Wedge fringe interferograms

The Mach-Zehnder interferometer is not always used with the two interfering wavefronts parallel to each other, as in the infinite-fringe setting discussed above. There is a second mode in which the two interfering wavefronts have a small angle θ between them, introduced deliberately during alignment. Upon interference they produce an image consisting of bright and dark fringes, representing the loci of constructive and destructive interference respectively. These parallel and equally spaced fringes are referred to as wedge fringes. The spacing between the wedge fringes is a function of the tilt angle and the wavelength of the laser light used, and is given by

$$d = \frac{\lambda/2}{\sin(\theta/2)}.$$

For small tilt angles, the above expression becomes

$$d \sim \frac{\lambda}{\theta}.$$

As θ is decreased to zero, the wedge fringes get farther apart, approaching the infinite-fringe pattern.

When a thermal or concentration field is introduced in the path of the test beam, the phase of the test wavefront gets distorted. Upon interference with the reference wavefront, it manifests itself as a change from straight and parallel fringes to curved fringes. The two interference patterns are shown schematically in Figure 9 and as an exploded view in Figure 10.
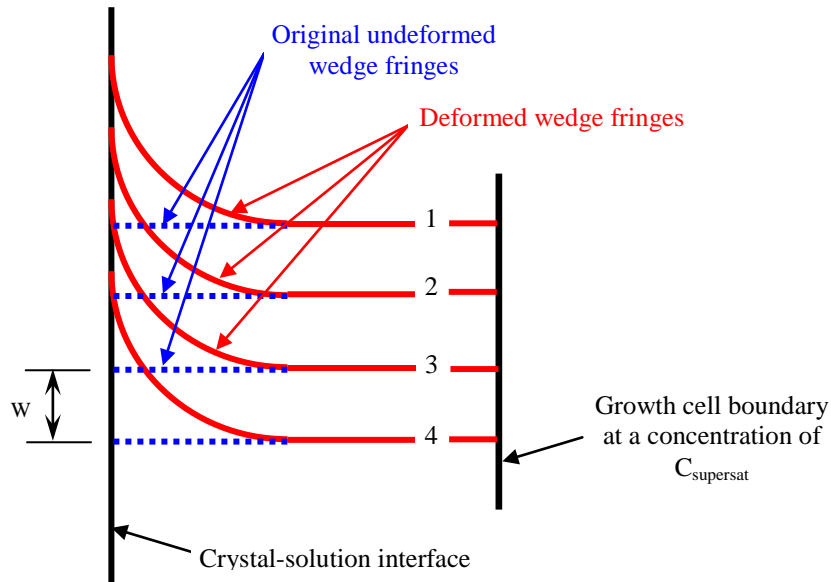

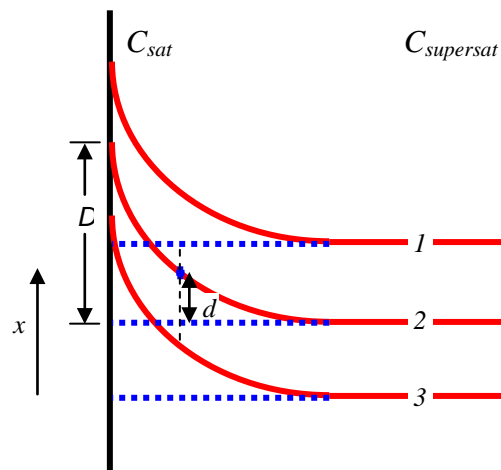Figure 9: Wedge fringe pattern with and without the field of disturbance.

Figure 10: Computing field concentration in the presence of the wedge fringes.

Let us develop a procedure to the solutal concentration at a point *x* in the interferogram. The deviation of fringe 2 near the crystal-solution interface is *D*, while at point *x* is *d*. Thus it can be written as [Goldstein, 1996]

$$\frac{C(x) - C_{\text{sat}}}{C_{\text{supersat}} - C_{\text{sat}}} = \frac{d}{D}$$

Since all other parameters except $C(x)$ are known, the local concentration can be easily calculated. The concentration gradient dC/dx is obtained from the slope of the fringes at a point *x*. The above methodology is used for calculating the concentration at points which lie on the wedge fringes. However, if one were to find concentration at a point lying between two wedge fringes, then one has to locate four nearby points on the wedge fringes and compute their respective concentrations. It is then followed by using a suitable interpolation technique to find the concentration at the desired point.

1.4.4 Holography and holographic interferometry

Holography is a form of interferometry and can be used to achieve new modes of measurement, for example, interference of images of the same object at two different points in time. We explain the conventional holography and how it differs from the holographic interferometry. Also various types of holographic interferometry are discussed.

Holography was discovered by Dennis Gabor in 1948 [Gabor, 1948 & 1949] and is based on the principles of interference and diffraction. Ordinary photography records only the wave intensity while the phase information is lost. In contrast, both the amplitude of the object wave and the phase are recorded in holography [Collier, 1971; Hariharan, 1986 & 2002]. Briefly, the procedure for hologram recording and subsequent reconstruction of the object image is as follows: A coherent beam of light from a laser is split into an illumination beam and a reference beam. The former illuminates the object so that the scattered light from the object strikes a high-resolution photographic plate. The reference beam is also reflected onto the photographic plate, where it interferes with the light from the object. The photographic plate, or *hologram*, is then developed to reveal the interference pattern registered on it.

The object wave can be reconstructed in two different ways, one resulting in a *virtual* image and the other in a *real* image. When the hologram is illuminated by the original reference

beam, the interference pattern on it behaves as a diffraction grating, and diffracts the incident light. A part of the diffracted beam is a replica of the object-image wavefront. By looking through the hologram into the direction of the original object, the viewer perceives the waves to be originating from a virtual image of the object located precisely at the original location (Figure 11a). On the other hand, if the back of the hologram is illuminated by a *conjugate* of the reference beam (a beam identical in phase and intensity distribution to the original reference beam but propagating in the opposite direction), the diffracted beam is directed and shaped by the hologram into a real image, corresponding spatially to the original object. Viewing in the direction of the diffracted beam recreates the object through the hologram (Figure 11b).

Holographic interferometry is a refinement of holography [Vest, 1979]. The main difference between classical interferometry and holographic interferometry is that for ordinary interferometry, an object wavefront is continuously compared against a reference wavefront, and the optical path length difference between the two wavefronts is measured to determine changes in the physical parameter of interest. In holographic interferometry, two types of interference phenomena occur - the interference between the reference and the object waves to form a hologram and the interference between two such holograms. This is equivalent to the interference of two coincident images of the same object at two different times. Thus, in classical interferometry, the two waves follow different paths at the same time while in holographic interferometry, they pass through the same path at two different times.

The reader is referred to the edited volume by Mayinger [Mayinger, 1994] and the review by Verma & Shlichta [Verma, 2008A] for details of different types of holographic interferometry. The three forms of holographic interferometry are explained schematically in the Figures 12(a-c). The three holographic interferometric techniques described above have several trade-offs. In the first, one follows the process in real-time, but provides only averaged parameter values along a single direction. The second technique is simple in implementation but provides the parameter values at a particular instant and also provides only averaged values along a single direction. The third can provide a three-dimensional array of parameter values, but again only at a particular instant of time.
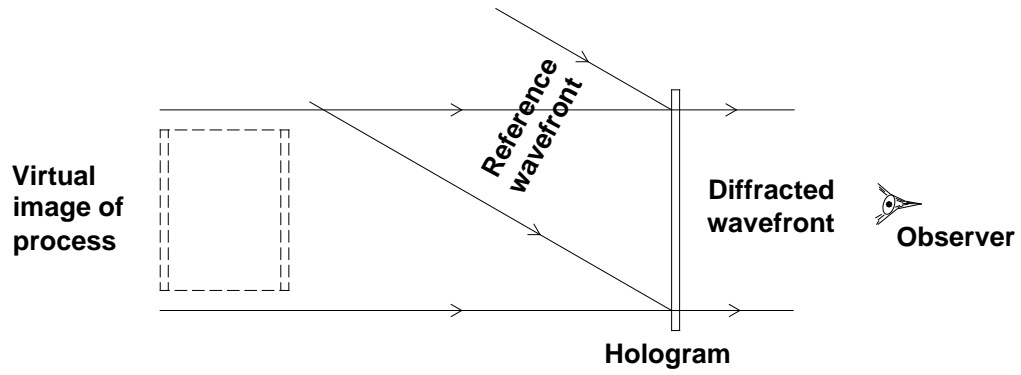
(a)
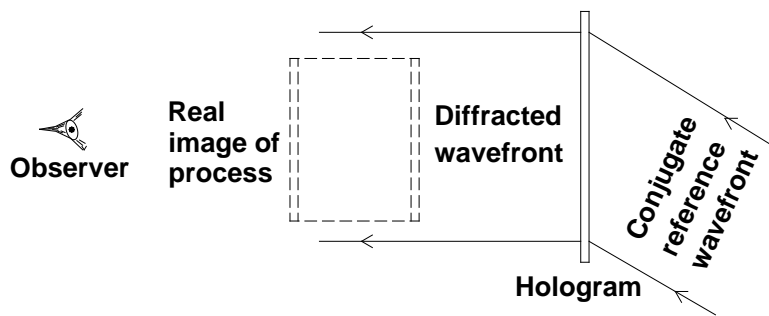
(b)

Figure 11: (a) Formation of virtual holographic image with original reference beam used for reconstruction, and formation of a real holographic image with a conjugate reference beam used for reconstruction [Verma, 2008].
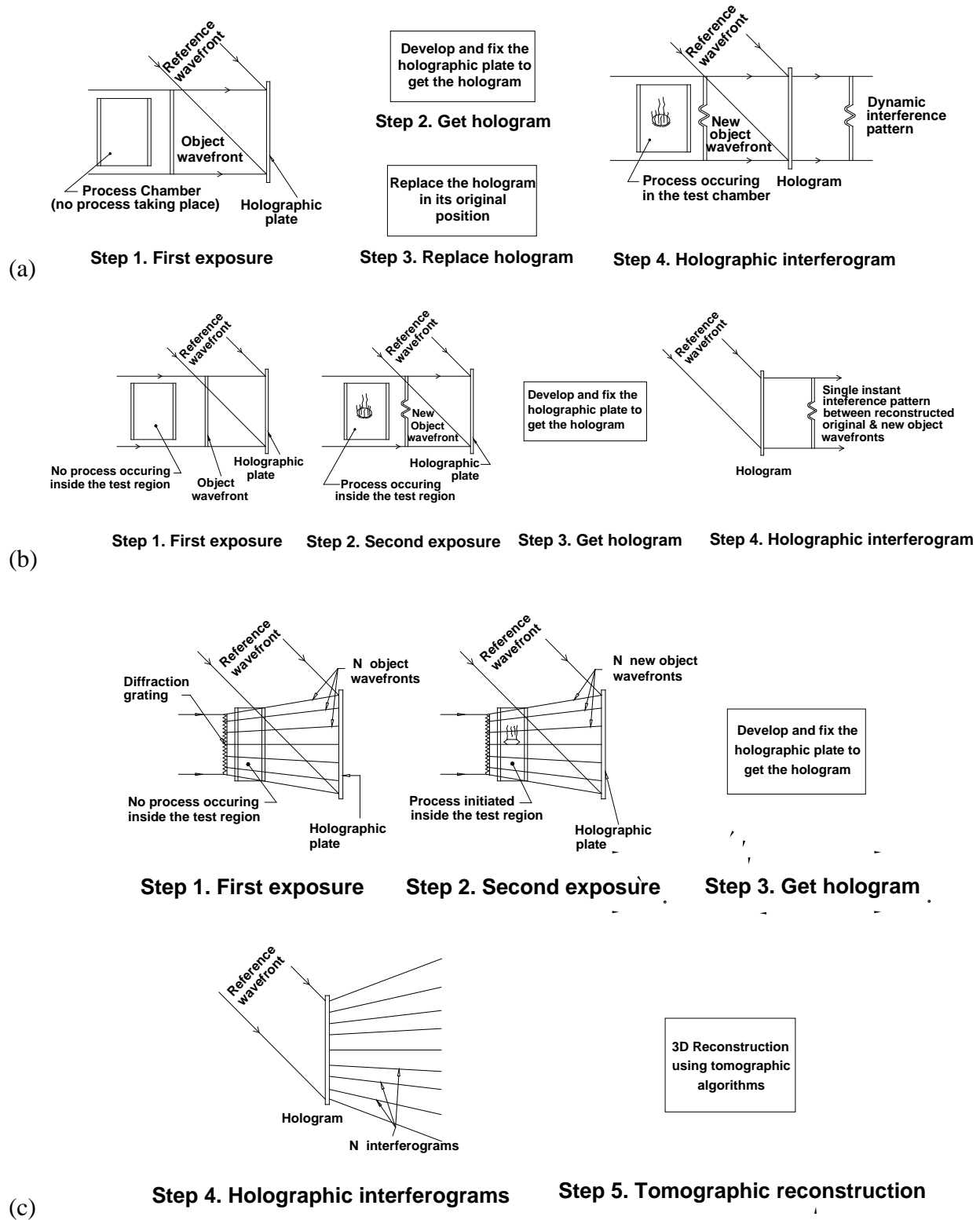
Figure 12:(a) Single-direction, single-exposure, real-time holographic interferometry, (b) single-direction, double-exposure, single-instant holographic interferometry, and (c) multi-directional, double-exposure, single-instant holographic interferometry and tomography [Verma, 2008].

1.5 Imaging heat transfer and mass transfer

Virtually all of the quantitative refractive index mapping techniques discussed thus far apply to the mapping of both, the heat transfer as well as the mass transfer fields. It is assumed that the experiment is essentially two-dimensional along the optical axis, so that the refractive index is constant along each ray of light. Further, an equation that connects refractive index with temperature (via density) is required to convert refractive index into absolute temperature. Interferometry can measure temperature in the following cases: (a) pure liquids having an appreciable dn/dT, (b) systems where changes in concentration are zero or negligible, and (c) applications where a second technique maps the solute concentration.

1.5.1 Mach-Zehnder interferometry

Mach-Zehnder interferometry can be employed for mapping heat and mass transfer. The quantitative methodology for extracting the field parameter (either temperature or concentration) from wedge- or infinite-fringe mode Mach-Zehnder images has already been discussed in the previous section. Mathematically, let *n(r)* and *T(r)* be the refractive index and temperature fields respectively, in the physical domain being studied. Let n_o and T_o be their reference values, as encountered by the reference beam. The interferogram is a fringe pattern arising from the optical path difference:

$$\delta = \int (n - n_o) dx$$

which, in terms of temperature is

$$\delta = \frac{dn}{dT} \int (T - T_o) dx \ .$$

Here the integration is over the path along the ray direction. Other forms of single-pass interferometry and holography can also be used and interpreted in an identical manner. The principal problem with interferometry, for both heat and mass transfer mapping, is calibration. This will not matter for fluid flow (convection) mapping because one is interested in having an observable difference between the moving and static parts of the fluid. Even when experiments require relative temperature or its gradients, the equation relating refractive index to temperature (or density) is required. Such a relationship is unique and obtainable for transparent media via the simplified Lorenz-Lorentz formula

$$\frac{n^2 - 1}{\rho \ (n^2 + 2)} = \ \text{constant} \ (k)$$

The material density can then be related to solute concentration and temperature. For a discussion on the generalized relationship, please refer [Kumar, 2008].

1.5.2 Phase shifting interferometry

Conventional interferometric mapping is based on obtaining an interferogram, locating the centers of the fringes, measuring the difference between the fringe-center position with that of the reference pattern, and finally interpolating between the fringes to obtain the variable of interest anywhere in the field. This procedure has the shortcomings of being tedious and time consuming and entailing a potential inaccuracy in locating the centers of fringes. Moreover, the data is localized at the fringes, which are often irregular in shape. It necessitates the process of transferring data to a regular grid by the interpolation procedure. The procedure of interpolation also can potentially introduce numerical errors.

Phase-shifting interferometry (PSI) can be used to circumvent the difficulties referred above. First developed by Bruning [Bruning, 1974], PSI involves (a) shifting the phase of one of the two interfering beams so as to get a sequence of phase-shifted interferograms and (b) data reduction to obtain the phase information. Several authoritative reviews exist on phase shifting interferometry [Creath, 1986, 1987 & 1988; Greivenkamp, 1992; Cloud, 1995] and are adopted here in explaining the evaluation steps involved. In general, phase shifting technique can be incorporated into any type of interferometer system. The phase of the reference beam is shifted with respect to that of the object beam in steps of $\pi/4$ or $\pi/2$ to get a sequence of phase-shifted interferograms. Various techniques are available to achieve the phase shift [Wyant, 1975 & 1978; Shagam, 1978]. These include mounting the reference mirror on a piezoelectric transducer that moves linearly in proportion to the applied voltage [Wyant, 1982 & 1985].

There are several algorithms reported in the literature for determining the phase of the interferogram using PSI [Creath, 1986 & 1988]. A minimum of three phase-shifted interferograms is required for determining the phase of the object wavefront. This is because the interference equation

$$I = I_{ref} + I_{obj} + 2\sqrt{I_{ref} \times I_{obj}} \ \cos(\phi_{ref} - \phi_{obj})$$

involves three unknowns, the reference and object beam intensities, and the phase difference between the two interfering beams. The following three-step technique serves as an example:

Let the phase shift between successive interferograms be $\pi/2$ and the absolute phase for the three interferograms be $\theta_1 = \dfrac{\pi}{4}, \theta_2 = \dfrac{3\pi}{4}$ and $\theta_3 = \dfrac{5\pi}{4}$. The set of three equations representing the phase-shifted interferograms are solved simultaneously to get the phase at each point as

$$\phi(x, y) = \tan^{-1}\left\{ \frac{I_3(x, y) - I_2(x, y)}{I_1(x, y) - I_2(x, y)} \right\}.$$

Therefore, by detecting the intensity modulation at each pixel and taking the above ratio, the phase at each point of the wavefront is determined.

PSI involves an additional procedure to be performed on the phase calculated through the arctangent equation in order to get the correct final description of the phase. This is necessitated by the nature of the arctangent function, which lies between $-\pi/2$ to $+\pi/2$. As a result, phase values fall within $\pm\pi/2$ regardless of the actual spread of the phase. Therefore arctangent calculations result in a wrapped up phase. The numerical process of phase unwrapping is carried out in two steps:

(1) Obtain the phase values through the arctangent equation that are confined within $\pm \pi/2$. Noting the discontinuity at every $|\pi/2|$ value, extend these values to fall between $-\pi$ and π. The phase obtained after this step is referred to as modulo 2π phase, and show discontinuity after 2π radians.

(2) Remove the 2π discontinuities by staring from end of the image in order to obtain a true and continuous map of the wavefront phase.

The phase map obtained by the above procedure is displayed as a gray image wherein the gray value of each pixel corresponds to the phase value at that point. Using 8-bit digitization the total phase shift (0 to $2n\pi$) is represented quantitatively by gray values in the range of 0 to 255. Using higher bit digitization could further enhance the resolution of the phase measurement, and as a result the resolution of the physical property being measured.

For PSI based on Mach-Zehnder interferometry, the change in refractive index $\Delta n(x, y)$ corresponding to the phase change of $\Delta\phi(x, y)$ is

$$\Delta n(x, y) = \frac{\lambda}{2\pi L}\Delta\phi(x, y)$$

where L is the length of the chamber through which the beam traverses. In order to get an idea of the resolution of the PSI, a calculation with typical values of parameters in the above equations will show that for a gray value change of unity between adjacent pixels, the minimum detectable Δh and Δn is 1 nm and 10^{-5} respectively. They are an order of magnitude higher than what is possible with conventional interferometry. It can be further increased by an order of magnitude if 9 or 10 bit digitization is employed.

Finite time is required for translating the reference mirror mechanically in order to obtain the phase shifted interferograms. Thus, conventional phase shifting interferometry has the limitation of being unable to follow a process in real time. Nakadate et al. [Nakadate, 1990 & 1995] overcame this limitation ingeniously by employing polarized light to simultaneously record the required number of phase-shifted interferograms.

1.5.3 Electronic speckle pattern interferometry (ESPI)

When a rough surface is illuminated with a coherent radiation, each facet of the object scatters radiation towards the observer/detector. Here rough stands for random and microscopic variations of height on the surface of the object with dimension more than the wavelength of light. Since the phase of the light scattered will vary from point to point in proportion to the local surface height, interference occurs between the light scattered from any two facets. Owing to the superposition of individual interference patterns, each arising from a separate facet on the rough surface, a random pattern of interference fringes, called *speckle* is observed. For a detailed discussion on the speckle phenomena, the reader is referred to [Dainty, 1984].

Electronic speckle pattern interferometry (ESPI) has been used for measuring concentration gradients. It can also be used to visualize convection in the form of variations in refractive index in the solution. This technique can be adapted for mapping temperature as well as convection patterns in fluids [Dupont, 1995; Verga, 1997]. In these applications, the speckle pattern is obtained by means of a stationary ground glass plate. When a chamber containing the fluids is interposed between the plate and the CCD camera, the optical path length is altered and a speckle interference pattern of the experiment is obtained. As the optical properties of the fluid in the chamber change, for example, due to changes in temperature, the phase of the speckle pattern changes. It results in changes in the interference pattern between the object and the reference speckles. This is subtracted from the speckle-interference-pattern recorded at the start of the

experiment to get the phase variation produced during the time interval. Thereby the spatial change in the field parameters such as refractive index and temperature are determined.

1.6 Simultaneous mapping of heat and mass transfer

In single-wavelength interferometry, the interpretation of the fringe pattern becomes difficult when two independent quantities (such as temperature and concentration) affect the phase of the traversing beam. The analysis is then based on the approximation that one of the two parameters has a negligible influence on phase. The approximation may not be not valid in certain processes wherein heat (temperature) and mass transfer (concentration) simultaneously affect the refractive index of the aqueous solution and hence the phase of the beam traversing the crystallizer. Here we need a diagnostic that can simultaneously map the two parameters. Dual-wavelength interferometry is capable of detecting temperature and concentration and is described below.

1.6.1 Dual-wavelength interferometry

Dual-wavelength interferometry can separate the influence of the two competing parameters such as temperature and concentration, provided the sensitivities dn/dC to dn/dT are significantly different for the two wavelengths. This problem is similar to solving two equations for two unknown variables. Using two different wavelengths for mapping the process results in two independent fringe patterns. Dual-wavelength interferometry was first used by El-Wakil and Jaeck to study heat and mass transfer in gaseous boundary layers [El-Wakil, 1964]. Later, Ecker proposed the concept of holography in conjunction with dual-wavelength interferometry for measuring temperature and concentration fields during alloy solidification [Ecker, 1987 & 1988]. Mehta (1990) and Vikram et al. (1990) reported the applicability of this technique for determining the temperature and concentration fields inside liquids. The principle of dual-wavelength interferometry (and holography) as explained in a few reports by Vikram and co-workers [Vikram, 1992A] is described below.

For processes influenced simultaneously by the temperature and the concentration fields, the total change in refractive index can be expressed as

$$\Delta n = \frac{\partial n}{\partial C}\Delta C + \frac{\partial n}{\partial T}\Delta T$$

where ΔC and ΔT are the changes in the concentration and temperature fields influencing the refractive index field respectively. Combining the two equations given above, we get

$$\frac{N\lambda}{L} = \frac{\partial n}{\partial C}\Delta C + \frac{\partial n}{\partial T}\Delta T .$$

Extending the above discussion to the dual-wavelength interferometry, we get two independent equations corresponding to the two source wavelengths, λ_1 and λ_2, which are then solved for independent estimates of the thermal and the concentration variations [Vikram, 1992A]. Thus

$$\Delta C = \frac{N_1\lambda_1 \dfrac{\partial n_2}{\partial T} - N_2\lambda_2 \dfrac{\partial n_1}{\partial T}}{L\left[\dfrac{\partial n_1}{\partial C}\dfrac{\partial n_2}{\partial T} - \dfrac{\partial n_2}{\partial C}\dfrac{\partial n_1}{\partial T}\right]}$$

and

$$\Delta T = \frac{N_1\lambda_1 \dfrac{\partial n_2}{\partial C} - N_2\lambda_2 \dfrac{\partial n_1}{\partial C}}{L\left[\dfrac{\partial n_1}{\partial T}\dfrac{\partial n_2}{\partial C} - \dfrac{\partial n_2}{\partial T}\dfrac{\partial n_1}{\partial C}\right]} .$$

For accurate determination of ΔC and ΔT, we must know precisely the refractive index and its gradients with respect to temperature and concentration at both the wavelengths and the fringe order. In the absence of experimental values, a suitable analytical methodology has been put forth by Vikram and co-workers [Vikram, 1991, 1992B] for determining the needed data. The refractive index is obtained using the two-constant Cauchy equation. A higher order Cauchy equation involving more constants may be used for greater accuracy. The refractive index gradients with respect to temperature and concentration are determined using Murphy-Alpert [Murphy, 1971] and Lorentz-Lorenz relationships respectively.

1.7 Computerized tomography

Since conventional optical techniques can only measure the average refractive index along the optical path (e.g. the thickness of the process chamber), quantitatively meaningful results are possible only in the following situations: Either the experiment is "two-dimensionalized" so that the parameter of interest is constant along the optical path; or truly three-dimensional imaging techniques are adopted for experimentation, such as holography [Gabor, 1948 & 1949; Hariharan, 1986 & 2002] for a direct 3-D imaging or computerized tomography for an indirect 3-D

visualization from a set of two-dimensional projection images. The principle of holography and holographic interferometry has already been discussed in section 1.4.4 of this chapter. The principle of tomography is briefly presented below.

Computerized tomography is defined mathematically as the process of constructing a continuous two-dimensional function from its one-dimensional line-integrals obtained along a finite number of lines at known locations [Ramachandran, 1971; Herman, 1980; Natterer, 2001]. This can be extended to include reconstruction of a three-dimensional function from its two-dimensional projections taken along a fixed number of known directions. Tomography is essentially a two-step process: first, collecting the projection data and second, reconstructing the three-dimensional function using numerical algorithms.

The tomographic reconstruction methods can be broadly classified as (1) transform methods, (2) series-expansion methods, and (3) optimization methods. The transform methods are computationally efficient, but require a large number of experimental projections to recover the process parameter with some satisfactory accuracy [Lewitt, 1983]. In contrast, the series expansion methods are computationally intensive, but have the advantage of giving satisfactory result even with limited or partial projection data [Censor, 1983]. The optimization approach requires the selection of a suitable functional that has to be extremized, under the experimental constraint [Gull, 1986].

Various forms of optical tomography have numerous potential applications in many diverse fields of science and engineering. We shall confine our discussion here to the application of shadowgraphic and interferometric tomography to the study of transport processes. In these cases, the line integrals of refractive index can be converted to point-by-point maps of refractive index at selected planes.

1.7.1 Shadowgraphic tomography

A three-dimensional pattern of varying refractive index inside the process chamber results in light rays getting refracted out of their original path. This caused a spatial modulation of the intensity distribution with respect to the original intensity and produced a shadowgraph pattern on the screen. Shadowgraph images recorded from several view angles constitute the experimental projection data. The intensity of each pixel in the shadowgraph images is processed numerically to extract the refractive index distribution. This constitutes the numerical input to the

reconstruction algorithms. It should be noted that refractive index distribution has one-to-one correspondence with the physical parameter, such as temperature, concentration or fluid flow field in the process chamber. The output of the tomography reconstruction algorithms is a matrix representing the process parameter values over a particular plane in the region of interest. A detailed discussion on the application of shadowgraphic tomography to the process of crystal growth can be found in the work of Verma et al. [Verma, 2006 & 2008B].

1.7.2 Interferometric tomography

In case of interferometric tomography, the projection data is in the form of interferograms captured from several angular directions. For example, a Mach-Zehnder interferometer can be used to capture interferograms of the process from several coplanar viewing directions. Such infinite (or wedge) fringe interferograms recorded nearly simultaneously from different view angles constitutes one set of 2D projection data. These interferograms are numerically processed to get the refractive index distribution, which serve as input to the tomography algorithms. It should be noted that data reduction in case of shadowgraph images is two orders of magnitude difficult as compared to interferograms due to analytical expression relating intensity with the refractive index field in the two processes. Finally, the methodology of implementing the reconstruction algorithms for interferometric tomography is similar to that for shadowgraphic tomography. Reader is referred to Mishra et al. [Mishra, 1998 & 1999] and Muralidhar [2001] for in-depth details of interferometric tomography as applied to heat transfer problems.

1.8 Comparison of optical techniques

Each technique described above is accompanied by certain advantages and weaknesses. Shadowgraph and schlieren have the advantages of low cost, ruggedness and simplicity of apparatus, and ease of real-time qualitative interpretation. Gradient interferometers provide an attractive trade-off between simplicity and versatility. Two-beam interferometers are probably the easiest to setup and permit quantitative information. Reconstructive holography has the important advantage of providing rich three dimensional detail. With regard to sensitivity, an analysis provided in pp. 150-155 of [Merzkirch, 1974] indicates that schlieren, gradient interferometry and two-beam interferometry all have about the same order of magnitude of sensitivity (about $\lambda/100$). The trade-offs between conventional and holographic interferometry

are particularly complex. Since holographic interferometry operates in a time-differential, rather than space-differential, manner, it has several advantages over classical interferometry. Unlike the latter, it does not depend critically on the alignment of the two interfering beams. Moreover, the need for high quality optical components is much less critical. Holography also provides capabilities not possible with conventional schlieren and interferometry. A collimated-beam hologram can be made of an experiment and then reconstructed into a real image that can then be processed at leisure to generate schlieren and gradient-interferometric images of variable orientation and fringe width [Smigielski, 1970; Merzkirch, 1987]. By using stored-image holography or by making time-lapse double exposures on the given holographic plate, interferograms which image the change in optical path length with time can be generated [Heffinger, 1966]. All these advantages, however, must be weighed against the disadvantages of lack of real-time viewing, labor of reconstruction, and incompatibility with simultaneous mapping of concentration and temperature fields. Electronic-speckle pattern interferometry is different from other interferometric and holographic techniques, in that it can be used under ordinary room lighting conditions. It does not require vibration isolation tables [Lokberg, 1980; Jones, 1989]. Although it is less sensitive to temperature/concentration changes compared to the conventional techniques of interferometry and holography, it can provide useful data under non-ideal laboratory conditions. Since ESPI functions as a time-difference interferometer it is similar to holographic interferometry. Hence, it does not require accurate adjustments of the interfering beams. Unlike holographic interferometry, it has the advantage that the information is directly recordable onto the CCD sensor without any intermediate recording plate. The primary drawback is the fringe quality, which is quite noisy due to the speckle property itself. As a result, the spatial resolution of the camera limits the resolution of the measurement.

2. APPLICATIONS

The second part of the chapter describes various applications of the above techniques in studying transport phenomena as encountered in engineering applications. These are: (i) crystal growth from solution [Verma, 2007, 2008 & 2009; Dinakaran, 2010], (ii) heat conduction phenomenon in a differentially heated layer of water [Singh, 2009], (iii) mass transfer from high concentration region to low concentration (dissolution of sugar) [Bhandari, 2009], (iv) natural convection in a differentially heated rectangular cavity of square cross-section (hot lower wall and a cold upper

wall) filled with air [Muralidhar, 2005], (v) buoyancy-driven convection in an octagonal cavity half-filled with 50 cSt silicone oil, the rest being air [Punjabi, 2002], (vi) long-time interferograms formed in an octagonal cavity containing silicone oil (50 cSt) floating over water [Punjabi, 2004], (vii) buoyancy-driven convection in a differentially heated cavity that is rectangular in plan (Rayleigh-Benard configuration) [Mishra, 1998], (viii) convection in an eccentric annulus with the gap filled with air [Ranjan, 2005], (ix) steady state heat transfer in an eccentric annulus when the gap is filled with 390 cSt silicone oil [Ranjan, 2005], and (x) convection and heat transfer behind heated circular cylinder at low Reynolds numbers [Singh, 2007].

2.1 Transport phenomena during crystal growth from solution

Crystal growth from solution is the most widely used method for growing large crystals, several centimeters in size [Mullin, 2001]. It is applicable to all classes of materials, including inorganic, organic, metal-organic, macromolecules and complexes. Solution growth offers the convenience of low operating temperatures, less complicated apparatus, and simple instrumentation. More importantly, when the process to be imaged uses optical radiation, the medium under study has to be necessarily transparent at the chosen wavelength of radiation (He-Ne laser wavelength in our experiments). Among the various methods of growth, only solution growth satisfies this requirement. For these reasons, the present work is primarily focused on crystal growth from solution. An ensemble of crystals grown using solution growth are [Paschotta, 2008]: KDP (potassium dihydrogen phosphate, KH_2PO_4) and its deuterated analogue DKDP (KD_2PO_4) for frequency conversion and electro-optic switching (Q-switches and Pockels cell) respectively; TGS (triglycine sulphate) for laser-energy measuring devices; KAP (potassium acid phthalate) for monochromator applications; $LiIO_3$, ZTS [zinc tris (thiourea) sulphate], and many organic and metal-organic crystals for linear and non-linear optical applications.

2.1.1 Importance of mapping solution growth

The ultimate goal of research on crystal growth is to achieve an in-depth understanding of the process with the aim of improving the microscopic and macroscopic homogeneity of the grown crystals, in addition to increasing their size. A crystal growing from solution creates thermal and concentration gradients in the surrounding solution by releasing the heat of crystallization and

depleting the solute near the growth surface. The resultant temperature and concentration gradients affect the perfection and stability of the crystal grown [Bunn, 1949]. The change of solution density with temperature ($d\rho/dT$) is negative and the change of solution density with solute concentration ($d\rho/dC$) is positive. Therefore, crystal growth in the Earth's gravitational field is accompanied by a rising buoyant convection current which envelops the crystal, is often oscillatory and unstable, and therefore drastically modifies the concentration gradient along the growth interface [Chen, 1979A & 1979B]. Thus, the growth history and defect structure of the crystal is a function of the time-dependent spatial distribution of the convection patterns, and of the temperature and concentration profiles in the surrounding solution. Therefore, in order to learn how to grow large defect-free crystals, it is helpful to map the spatial distribution of thermal and concentration profile around the growing crystal.

2.1.2 Phenomenology of the growth process

The rate of crystallization is determined by its slowest stage. Two major stages can be identified: (1) supply of crystallization material from the solution to the crystallization surface; (2) incorporation of this material into the crystal structure, i.e. growth of the crystal. If the first stage is the limiting step, the growth is said to proceed in the *diffusion regime*. If the second stage is the limiting step, growth is said to be operating in the *kinetic regime*. Diffusion regime conditions are prevalent during free convection growth, also referred as buoyancy-driven growth. In practice, forced flow conditions are adopted. These conditions bring the process into the kinetic regime of growth and are achieved by employing various modes of stirring. Here the solute is forced to move from the bulk solution towards the crystal surface. There is increased probability of occurrence of defects under irregular or turbulent flow conditions. Under such conditions the growth rate is high. Therefore, the mass transfer and the fluid flow conditions have to be optimized to avoid deleterious effects such as morphological instability, spurious nucleation, and inclusions. Thus, of particular importance in crystal growth from solution are fluid flow, and heat and mass transfer. Before discussing the results of crystal growth imaging, it is pertinent that a brief description is given of the experimental steps involved in growing a crystal from its aqueous solution.

2.1.3 Supersaturation: Driving force for crystal growth from solution

The prerequisite for crystallization to take place is the creation of a suitable driving force for the nucleation to occur. In solution growth, this driving force is referred to as *supersaturation*. It is a state of the solution achieved by manipulating its thermal behavior. It can be achieved in the following three ways: (a) *Cooling*: Cooling a saturated solution will result in a supersaturated solution, (b) *Evaporation*: Evaporation of the solvent leads to an increase in concentration of the solution, leading to a supersaturated solution, and (c) at times, a combination of cooling and evaporation is adopted.

The supersaturated state is created by having prior information about the solubility of the material in an appropriate solvent. Solubility of a material in a solvent decides the amount of the material that can be dissolved in it at a particular temperature. If the solubility is too high, it is difficult to grow a large crystal from such a solution. This is because of its sensitivity to thermal fluctuations. At the same time, if the solubility is low, it restricts the growth of large crystals since enough solute is not available for crystallization. The solubility of the material is measured by dissolving it in a continuously stirred solvent; this is done at several temperatures. A relationship so obtained between concentration and temperature fields is referred to as the *solubility diagram*.

A small good quality crystal is used as seed for initiation of the growth. While immersing the seed crystal, the solution temperature is kept 0.5 degrees above its saturation value so as to dissolve a few surface layers of the crystal. The dissolution helps in the elimination of the physical imperfections on the crystal faces, and also of any surface contamination introduced during crystal processing. After dissolving the crystal for a few minutes, the solution is cooled to its saturation point. A programmed cooling of the solution with an appropriate cooling rate is given from this point onwards to continue the growth. The difference in the concentration at saturation temperature and the temperature at which the experiment is performed gives us the extent of supersaturation of the solution. This is the driving force for the growth process and is computed at each stage of imaging experiment.

2.1.4 Optical imaging of crystal growth from solution

Several research groups working in the field of thermal sciences have also used it for mapping convection during various engineering processes [Rasenat, 1989; Mayinger, 1993; Schopf, 1996;

Goldstein, 1996; Settles, 2001]. However, this technique has not been widely used for crystal growth studies. Shiomi et al. used shadowgraphy to measure the temperature profile around a growing Rochelle salt crystal [Shiomi, 1980], while Lenski et al. used a beam deflection technique to measure convection during vapor crystal growth [Lenski, 1991]. Recently, Verma et al. [Verma, S., 2003, 2005C & 2006] have used shadowgraphy for visualizing the buoyancy driven convective patterns around a growing KDP crystal, and studied the gradual build up of this activity with the dimension of the crystal and the time of the growth. A few representative images, shown in Figure 13, demonstrate that buoyant convection increases with the increase of the Grashof number, which is the fluid dynamical dimensionless number representing the strength of the buoyancy driven convection. With the progress of growth, the convection mode changes from laminar (Figure 13a) to chaotic (Figure 13f). The influence of free and forced convection, and the cooling rate on the growth rate and the quality of the grown KDP crystal has also been studied [Verma, S., 2007]. Recently, Dinakaran et al. studied the polar morphology of zinc tris (thiourea) sulphate (ZTS) crystals using this technique [Dinakaran, 2010]. The influence of growth geometry on convection and the morphology of the grown ZTS crystals is shown in time lapsed shadowgraph images shown in Figure 14.

The schlieren technique was used by Chen et al. measured the magnitude and stability of convection around growing sodium chlorate crystals [Chen, 1979A & 1979B]. Chen also studied the relationship between the convection irregularities observed over a growing sodium chlorate crystal, and formation of defects such as fluid inclusions [Chen, 1977]. Onuma et al. used schlieren techniques to study the buoyancy driven convection above a growing barium nitrate crystal [Onuma, 1988 & 1989]. Srivastava et al. used schlieren for visualizing convection around a growing KDP crystal [Srivastava, 2004].

Rashkovich and co-workers used a Mach-Zehnder interferometer to measure the diffusion boundary layer thickness under different flow velocities of the solution flowing past the vicinal facets of ADP and KDP crystals [Rashkovich, 1990A & 1990B]. Duan et al. used the high sensitivity of phase-shifting Mach-Zehnder interferometry to map minute convective features around a growing $NaClO_3$ crystal [Duan, 2001]. Recently, Verma et al. have used such an interferometer in both infinite-fringe-width and wedge fringe modes to study the convective field around a KDP crystal growing under free and forced convection conditions in both platform and suspended crystal geometries, and correlated their results with the growth rate and quality of

the crystal [Verma, 2005B & 2007]. Figure 15 shows the concentration gradient inside the crystallizer during KDP growth under buoyancy driven convection conditions. Due to the growth of crystal, a low density convection plume rises up from the crystal resulting in accumulation of low density solution in the upper part of the crystallizer as compared to the lower portion of the crystallizer. This results in a concentration gradient inside the crystal, which manifests itself in the form of horizontal fringes in case of infinite fringe Mach-Zehnder interferometric imaging. This condition is detrimental to the growth of good quality optical crystals and should be avoided.

Bedarida's group used transmission holographic interferometry as a tool for controlling $NaClO_3$ crystal growth by monitoring the convection around the growing crystal [Bedarida, 1977]. The Chinese group of Yu Xiling adopted real-time, single-exposure holographic interferometry for measuring the diffusivities of KDP and DKDP solutions as a function of temperature and concentration [Xiling, 1992]. The same technique was used to study the convection driven mass-transport processes at the solid-liquid interface during the growth of DKDP crystals [Xiling, 1996].

Optical techniques have been extensively used for imaging the process of crystal growth aboard space flights. For example, Owen and Shlichta constructed a multimode optical observation system (MOOS) for observing crystal growth process using schlieren, shadowgraphy, absorption and shearing interferometry aboard NASA space shuttle [Owen, 1975; Shlichta, 1985]. Owen also used a Mach-Zehnder interferometer and a holographic unit for studying the growth of NH_4Cl and TGS crystals under microgravity environment [Owen, 1982 & 1986]. Single exposure holograms were recorded to study the crystal profile microscopically; the interferometric data was used to obtain concentration and temperature profiles near to the crystal; double-exposure holographic interferometry was performed to obtain details of the refractive index changes occurring during growth; and the holographic images were used to observe the development of crystal morphology, growth rate, and the surface structure. Witherow used a multipurpose holographic system used for investigating the TGS crystal growth experiment aboard Spacelab3 [Witherow, 1987]. The methodology of generating shadowgraph, schlieren, and interferometric images of the growth process in a ground-based laboratory from the holograms recorded in space was also discussed. Solitro, Gatti, Bedarida, and their co-workers developed a fiber-optic based multidirectional holographic interferometer for monitoring convection during crystal growth in space [Solitro, 1989; Gatti, 1989; Bedarida, 1992]. The

special volume containing specific contributions dealing with the development of advanced optical diagnostics for crystal growth applications in space was compiled by Trolinger and Lal [Trolinger, 1991]. Experiments on later missions made use of phase-shift interferometry (PSI) and multicolor holographic interferometry (MCHI), developed at Space Sciences Laboratory of the Marshall Space Flight Centre (MSFC) for detecting the temperature and concentration field gradients during crystal growth [Witherow, 1994]. Dubois et al. describe the development of an integrated optical set-up for fluid-physics experiments, including crystal growth [Dubois, 1999]. The features of the schlieren technique, electronic speckle pattern interferometry (ESPI), differential interferometry, digital holography, and holographic interferometry were discussed. The performance of different diagnostics was compared for temporal resolution (the recording speed, which is dependent on the hologram refreshing rate), spatial resolution (sensitivity), and dynamic range, using the benchmark experiment of refractive index measurement in Rayleigh-Bénard instability.

The availability of high quality protein crystals is vitally important for determining their structure and subsequently for drug development [McPherson, 1982 and 2001; Ducruix, 1992]. Shlichta presented a summary of the optical techniques available for imaging crystal growth from solution in general, and for protein crystal growth in particular. The European Space Agency (ESA) has developed a Protein Crystallization Diagnostics Facility (PCDF) equipped with several optical imaging diagnostics for on-line and *in-situ* monitoring of the growth phenomena aboard the International Space Station (ISS) [Pletser, 2001]. Cole *et al.* mapped refractive indices around growing protein crystals by Mach-Zehnder interferometry [Cole, 1995]. McPherson et al. used a phase-shift Mach-Zehnder interferometer to observe the fluid environment around a growing protein crystal in the ground [McPherson, 1999] and in microgravity [McPherson, 2001]. Yin et al. used a Mach-Zehnder interferometer to study the influence of magnetic field on the convection, concentration, solubility and temperature during growth of lysozyme crystals [Yin, 2001 & 2003].

Several research groups have used Mach-Zehnder interferometer for solutal and thermal field studies of crystal growth process. Onuma et al. measured the surface supersaturation under different flow velocities of the solution flowing over the face of a growing K-alum crystal [Onuma, 1989]. Nakadate and Yamaguchi developed a real-time phase shifting Mach-Zehnder interferometer for concentration measurements [Nakadate, 1990], which was later adopted by

Onuma et al. and Kang et al. for concentration measurements around $NaClO_3$ crystal [Onuma, 1993; Kang, 2001]. Kim et al. used a similar interferometer to measure concentration variations at the interface between the solution and the crystal of L-arginine phosphate (LAP) [Kim, Y., 1998A]. Nagashima and Furukawa used this type of interferometer to study the solute distribution during directional growth of ice crystals, and to understand the origin of morphological instability leading to the dendritic growth [Nagashima, 2000]. Chen et al. used the Mach-Zehnder interferometer as an aid to monitor and control the growth of large size $NaClO_3$ crystals [Chen, 2002].

Verma et al. used a Mach-Zehnder interferometer in infinite and wedge fringe settings for mapping convection and concentration field [Verma, 2009]. Figure 16 shows infinite fringe and wedge fringe interferograms of a crystal growing under free convection conditions in top hanging geometry. The free convection plume and the diffusion boundary layer are clearly visible in infinite fringe interferograms but not in wedge fringe interferogram. Figure 17 shows infinite and wedge fringe interferograms of a crystal growing under forced convection conditions in top hanging geometry. No buoyancy driven convection plumes are visible as the crystal is rotating at high RPM and the concentration is uniform inside the crystallizer. Minor fringe distortion can be seen near to the crystal-solution interface. Figure 18 shows infinite fringe and wedge fringe interferograms of the crystal growing on a platform under free convection conditions. The concentration gradient is clearly visible in the third interferogram. The free convection plume and the diffusion boundary layers are visible in the infinite as well as wedge fringe interferograms.

Onuma et al. used the real-time phase shift interferometer, developed by Nakadate and Yamaguchi, to measure the concentration field around growing and dissolving $NaClO_3$ crystal [Onuma, 1993; Nakadate, 1990]. Maruyama and co-workers employed a real-time PSI to study the thermal and mass diffusion fields of the aqueous solutions of $NaClO_3$ and $Ba(NO_3)_2$ under microgravity conditions [Maruyama, 1999 & 2002]. Duan et al. used real-time PSI to map convection during $NaClO_3$ crystal growth [Duan, 2001]. McPherson et al. used a phase-shift Mach-Zehnder interferometer to observe the fluid environment around a growing protein crystal on the ground [McPherson, 1999] and in microgravity [McPherson, 2001].

Piano and co-workers have used speckle pattern interferometry for measuring the refractive index variation around a growing KDP crystal [Piano, 2000 & 2001]. The applicability

of dual-wavelength holographic interferometry for studying triglycine sulfate crystal growth has been discussed by Vikram and co-workers [Vikram, 1991 & 1992A]. Witherow et al. [Witherow, 1994] describes the efforts in combining the dual-wavelength interferometry with the phase-shifting interferometry for studying crystal growth experiments under microgravity environments.

2.2 Heat conduction in a horizontal fluid layer

Figure 19 provides snapshots of interferograms that reveal the heat conduction phenomenon in a differentially heated layer of water [Singh, 2009]. The container is a closed cavity, insulated on the sides, with the top surface maintained at 23^oC and the base at 18^oC. The room temperature during the experiments was maintained at 20^oC. The temperature difference creates a density field and in turn, a refractive index field, thus providing a basis for the formation of interferograms. Since fluids expand with an increase in temperature, the temperature differential creates a density stratified fluid layer, with hot fluid floating over the cold. The thermal field is imaged using a Mach-Zehnder interferometer in the infinite fringe setting. To set the interferometer initially, a compensation chamber filled with water at room temperature is used in the path of the reference beam. Since the surface temperatures are different from the initial value, fringes emerge from the top and the bottom till steady state is reached. Steady state is characterized by straight equi-spaced fringes. The fringe curvature during the initial stages could be the result of imperfect optical alignment that balances the arms of the interferometer. At later times, this error in units of optical path difference is small in comparison to the path difference created by thermal disturbances.

2.3 Dissolution of sugar in water

In Figure 20, a layer of sugar applied at the base of container is dissolving [Bhandari, 2009]. On evaporation of water, a layer of sugar adheres to the surface. Water is poured in the container till it gets filled. A compensation chamber is used to balance the arms of the interferometer and arrive at an infinite fringe setting. With the passage of time, sugar slowly dissolves in water. The concentration of sugar in water, thus, changes with time. It is accompanied by the appearance of interferometric fringes. Water adjacent to the lower wall has the highest sugar concentration, diminishing progressively towards the upper wall. During the transient phase, a layer of clear (sugar-free) water is obtained in the upper half of the cavity. Though the physical problem is

driven by mass transfer, the overall situation is analogous to heat transfer in a differentially heated cavity. There is point of difference, however. Sugar at the base creates a region of high concentration, high density and high refractive index while the other wall is one of zero sugar concentration, as in the compensation chamber. Thus, fringes originate from the lower wall alone.

2.4 Buoyancy-driven convection in a square cavity

Figure 21 shows natural convection in a rectangular cavity of square cross-section [Muralidhar, 2005]. The fluid medium in the cavity is air and convection is driven by the temperature differential between a hot lower wall and a cold upper wall. The side walls are insulated. Since the lower wall is heated, it is a region of low density when compared to the top surface. Thus, cold fluid is overlaid the hot in a gravitationally unstable configuration. The resulting fluid motion distorts the temperature distribution. When the temperature difference is large, the strength of fluid convection is great and large temperature changes occur close to the boundaries. This phenomenon is akin to the formation of boundary-layers - both hydrodynamic and thermal. The symbol Ra is Rayleigh number and is a measure of the strength of natural convection in the cavity. The first column carries interferometric fringes. The second and third columns contain a re-distribution of light intensity as obtained from schlieren and shadowgraph techniques. In schlieren, the initial light intensity is rather low but can be suitably adjusted. When the temperature differential across the fluid layer is turned on, regions of high temperature gradients are uniformly illuminated, with low gradient regions remaining dark. In a shadowgraph, the initial intensity distribution is set at a convenient initial value. Temperature gradients can result in either a local increase in intensity or a reduction all the way to zero. Thus, the intensity field may brighten or darken about the initial value. In addition, the resulting intensity of shadowgraph depends on the position of the screen.

2.5 Convection in a fluid layer with a free surface

Figure 22 shows buoyancy-driven convection in an octagonal cavity half-filled with 50 cSt silicone oil, the rest being air [Punjabi, 2002]. The cavity has eight sides and forms an octagon in plan. The lower surface is heated while the top surface is cooled. The thermal arrangement creates cold/heavy fluid at the top floating over hot/light fluid at the bottom, in a gravitationally unstable arrangement. Thus convection patterns are possible in both fluid layers – air and

silicone oil. However, the thermal conductivity of air is small when compared to silicone oil. Hence, a considerable fraction of the overall temperature difference occurs in oil and the temperature difference across air is negligibly small. Neither is air set in motion nor do clear fringes form in air. In contrast, convection is set up in silicone oil and fringes that are isotherms are deformed. The omega-shaped fringe (as well as others that are similar but show smaller deviation) is a result of projecting an axisymmetric thermal field along the viewing direction. Figure 22 shows interferometric projections of the refractive index distribution when the thermal field is viewed in various directions – 0, 45, 90, and 135°. Since the figures are practically identical, one may conclude that the thermal field does not depend on the polar angle and may be classified as axisymmetric.

2.6 Convection in a two-fluid layer system

Figure 23 collects long-time interferograms formed in an octagonal cavity containing silicone oil (50 cSt) floating over water [Punjabi, 2004]. Interferometric projections recorded from four different angles are shown. The flow is driven by an overall temperature difference, the lower surface being warmer than the top surface. Thus, cold/dense fluid set over warm/light fluid generates buoyancy forces and drives fluid convection. Water and oil are immiscible and independent convection patterns are set up in each part of the cavity. Since the fluid conductivities are comparable, a finite temperature difference is available across each fluid layer and detectable fluid convection is to be seen in each half. The overall temperature difference across the cavity is 1.8 K, the top plate being cooler than the one at the base. Of special interest are the energy and momentum transfer at the oil-water interface. When water is set in motion, it can drive the oil layer beneath even if buoyancy is absent. The underlying mechanism is viscosity and the fluid layers then said to be mechanically coupled. The other possibility is that each fluid layer experiences buoyant convection whose strength scales with the temperature difference appropriate for each of them. The fluid layers are then said to be thermally coupled. In the present experiment, interferometric images show that the nature of coupling is thermal in origin. In addition, the images look different in each view angle, indicating the onset of three dimensional velocity and temperature fields.

2.7 Rayleigh-Benard convection in a rectangular cavity

Figure 24 reports images and analysis related to buoyancy-driven convection in a differentially heated cavity that is rectangular in plan [Mishra, 1998]. The height of the cavity is small in comparison to the linear dimensions of the rectangle (around 10%). The lower surface is warmer than the top. The overall arrangement is the familiar Rayleigh-Benard configuration. The fluid medium considered is air. For temperature differences and cavity height considered, three dimensional fluid motion and temperature distribution are to be expected. The circulatory motion of the fluid particles creates a roll-type of motion. The roll patterns of the flow field are seen as fringe displacement in the interferograms. The corresponding interferograms seen from various viewing directions are shown in the figure. The schematic drawing at the top indicates how a roll is created within the cavity. Here, a parcel of warm fluid rises as a buoyant plume at a certain location, spreads on its way upwards, reaches the cold top, and descends downwards at a second location by gravity. Points where the fluid rises with those where the fluid descends together form a cellular pattern within the cavity. The geometry of the pattern can be understood by recording interferograms from various directions. A sample interferogram is shown in the figure. Here, fringe displacement upwards can be correlated with the rising buoyant plume. Conversely, fringe displacement downwards shows the descent of the cold fluid. The entire thermal field in can be reconstructed by a numerical procedure called tomography. Here, temperatures integrated along the viewing direction are required over the image as input data. An intermediate step that assists conversion of fringe patterns to temperature is fringe thinning. It replaces the fringe bands by a skeleton, using image processing techniques. A sample set of thinned interferograms is also shown in Figure 24, for various view angles.

2.8 Convection in an eccentric air-filled annulus

Figure 25 shows a time sequence of interferograms recorded in an eccentric annulus with the gap filled with air [Ranjan, 2005]. The axes of the two cylinders are horizontal. The cylinder length is roughly ten times the outer cylinder diameter. The inner cylinder is heated while the outer cylinder is kept at the ambient temperature. Heating is by an electric coil wound over a bakelite rod and covered by mica. The heating assembly is placed within the inner cylinder. Thermocouples have to be located over the cylinder length to ensure temperature uniformity along the axis as well as in the angular direction. Initially, the fluid in the annulus is also at the

ambient temperature. The fringes are recorded in the infinite fringe setting. Fringes originate from the inner heated boundary. For the temperature difference considered, density differences are large enough for buoyant convection to be set up in the annulus. The fluid is driven upwards near the inner cylinder and flows around the inner periphery of the outer cylinder during the descent. Thus, fringes show upward displacement closer to the inner cylinder. Owing to the eccentricity of the inner cylinder in its placement with respect to the outer, symmetry in the fringe patterns is broken. The stem attached to the inner cylinder holds it in place and is visible in the recorded images. The fringe patterns yield information on the distribution of heat flux around the inner cylinder. Here, the wall heat flux scales with the derivative of temperature in the radial direction. Since large derivatives will create closely spaced fringes, fringe spacing itself is indicative of the wall heat flux. The interferograms show that fringe spacing is small on the lower side of the cylinder and consequently, the wall fluxes are large. On the top side, fringe spacing is large and the wall fluxes can be expected to be small (in comparison). It is also to be understood that fringe thickness scales inversely as the local temperature gradient. Thick fringes are regions of low gradients. Thus, above the inner cylinder, one obtains a region of warm fluid of nearly uniform temperature.

2.9 Convection in an eccentric annulus filled with silicone oil

In Figure 26, interferograms recorded during steady state heat transfer in an eccentric annulus are presented when the gap is filled with 390 cSt silicone oil [Ranjan, 2005]. The applied temperature differences increase from 0.2 to 2 K while going from (a) to (e). When compared to air, several differences are to be observed in the fringe patterns. These include a substantial increase in the number of fringes. In addition, strong refraction errors are seen errors near the inner cylinder where the temperature gradients are large. However, the thermal fields retain symmetry about the position of the inner cylinder indicative of weak convection effects in the annulus. For small temperature differences, the buoyancy forces cannot overcome the viscous and the fluid is stationary. Heat transfer is then by conduction alone, as seen by near circular fringes for a temperature difference of 0.2 K. In liquids such as silicone oil, experiments with interferometry are to be carefully designed so that refraction errors are small and the fringe density is matched to the camera resolution.

2.10 Vortex shedding from a heated cylinder

Figure 27 shows instantaneous schlieren images for flow past a circular cylinder [Singh, 2007]. Wakes behind heated circular cylinders have been experimentally investigated at a low Reynolds number (100-300). The electrically heated cylinder is mounted in a vertical airflow facility such that the buoyancy aids the inertia of the main flow. The operating parameters, i.e. Reynolds number and Richardson number are varied to examine flow behavior over a range of experimental conditions from the forced to the mixed convection regime. Laser schlieren-interferometry has been used for visualization and analysis of the flow structures. At the Reynolds number studied, the unheated cylinder will periodically shed vortices. The complete vortex shedding sequence has been recorded using a high-speed camera. The results on detailed dynamical characteristics of the vortical structures i.e. their size, shape and phase, Strouhal number, power spectra, convection velocity, phase shift, vortex inception length and fluctuations are reported. On heating, the alteration of organized (coherent) structures with respect to shape, size and their movement is readily perceived from the instantaneous Schlieren images before they reduce to a steady plume. For the circular cylinder, Strouhal number shows a slow increase with an increase in the cylinder temperature, namely the Richardson number. At a critical value, there is complete disappearance of vortex shedding and a drop in Strouhal number to zero. The corresponding spectra evolve from being highly peaked at the vortex shedding frequency to a broadband appearance when vortex shedding is suppressed. The geometry of the vortex structures transforms to a slender shape before shedding is suppressed. The convection velocity of vortices increases in the streamwise direction to an asymptotic value and its variation is a function of Richardson number. The convection speed abruptly falls to zero at the critical Richardson number. The phase difference of the shed vortices between upstream and downstream location increases with an increase in Richardson number. Velocity profiles show an increase in fluid speed and beyond the critical point, buoyancy forces add enough momentum to cancel the momentum deficit due to the cylinder.
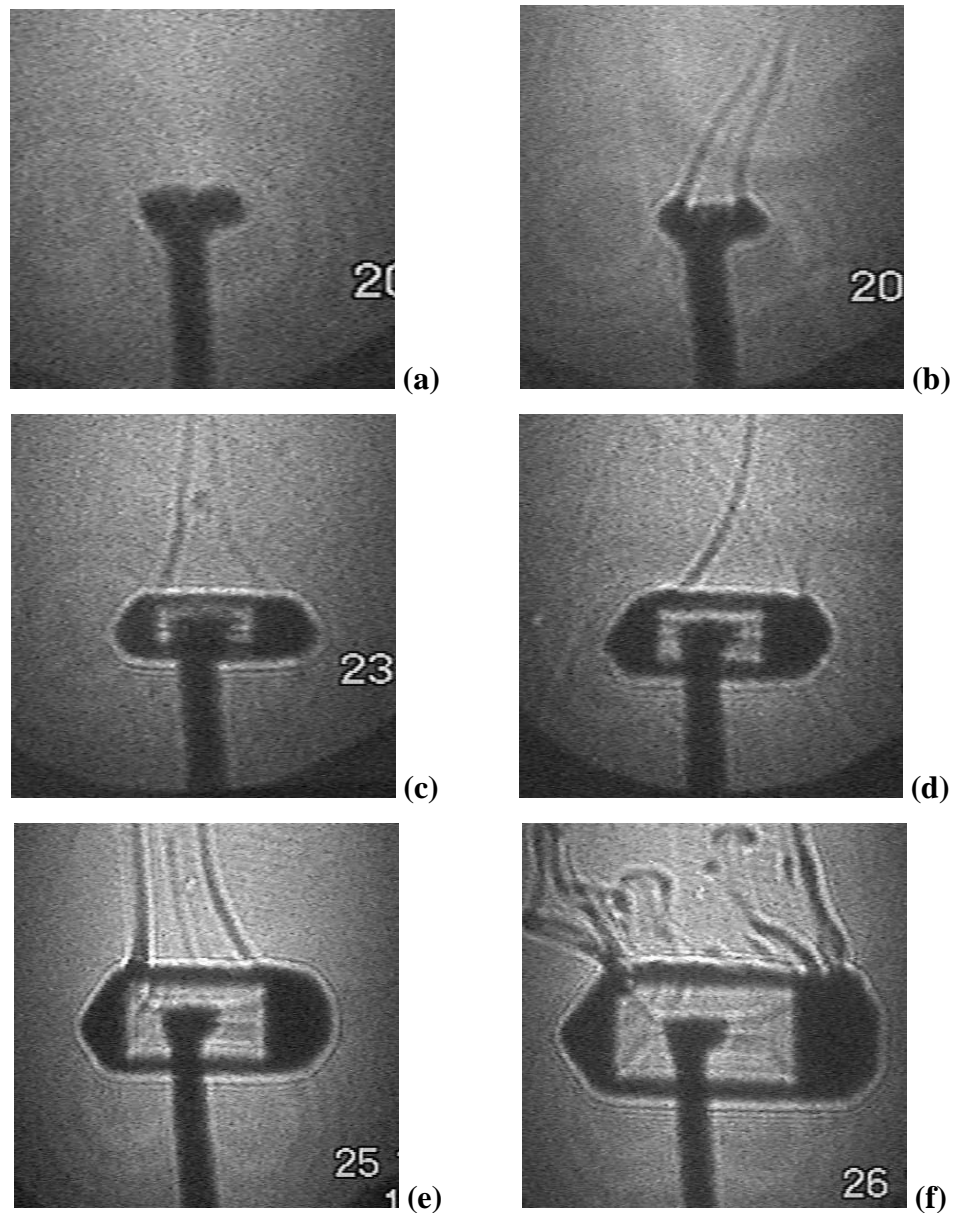
Figure 13: Shadowgraph images show an increase in the strength of buoyancy-driven convection with the growth of the KDP crystal. (a) No buoyant plume is seen at the start; (b) A stable plume start to appear as the growth begins; (c-e) Buoyant convection intensifies as the crystal grows; (f) The buoyant plume changes from laminar to irregular and finally becoming chaotic. Images adapted from *Imaging techniques for mapping of solution parameters, growth rate, and surface features during the growth of crystals from solution,* Sunil Verma and P.J. Shlichta, Prog. Cryst. Growth & Charact. Materials, 54 (2008) 1-120.
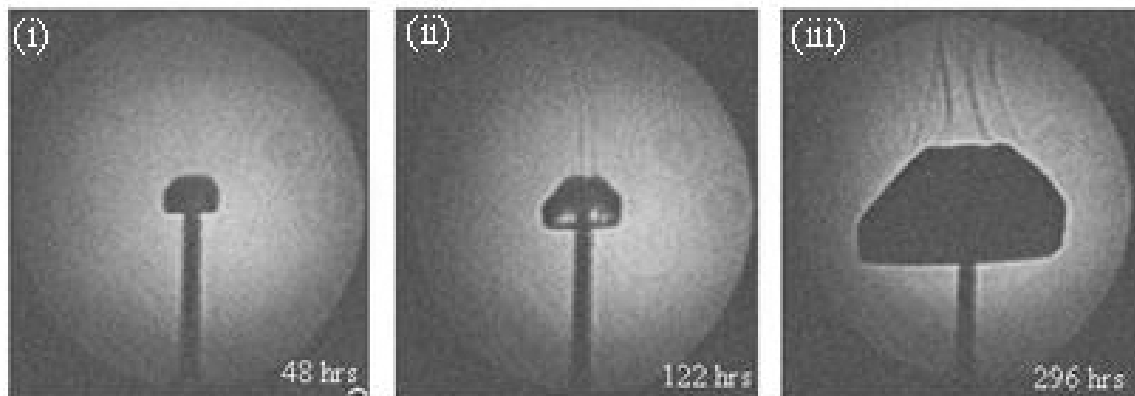
(a)
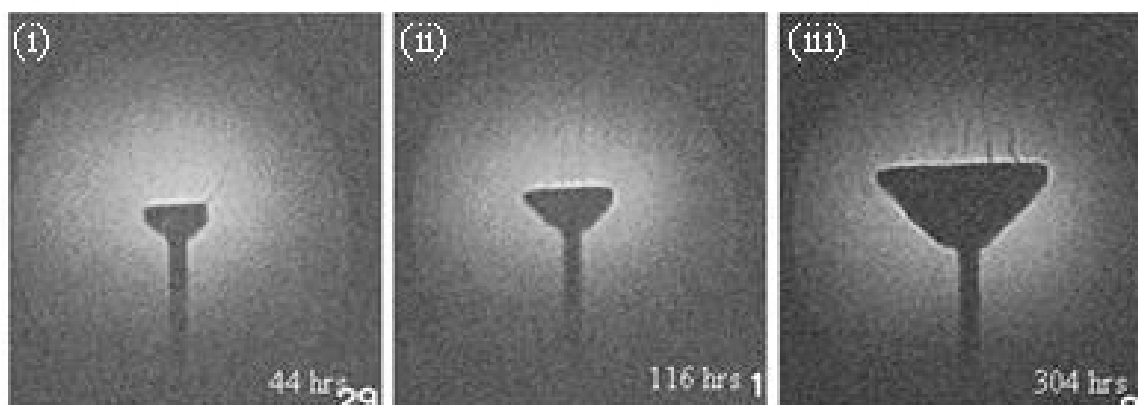
(b)

Figure 14: In order to measure the growth rates of {001} and {010} faces of ZTS crystals and their influence on the growth morphology, imaging was performed in two different growth geometries. In the first experiment, the seed was oriented such that (001) face was pointing upwards (a), whereas in the second the (001) face was pointing downwards (b). Shadowgraph images were recorded in a time lapsed manner for the entire duration of the two experiments. The images were used to calculate precisely the growth rates of {001} and {010} faces. Optical imaging helped in real-time and in-situ observation of the evolution of the growth morphology as a function of the growth geometry and supersaturation. Images adapted from *Optical imaging of the growth kinetics and polar morphology of zinc tris (thiourea) sulphate (ZTS) single crystals,* S. Dinakaran, Sunil Verma, S. Jerome Das, S. Kar and K.S. Bartwal, Cryst. Res. Technol. 45 (2010) 233-238.
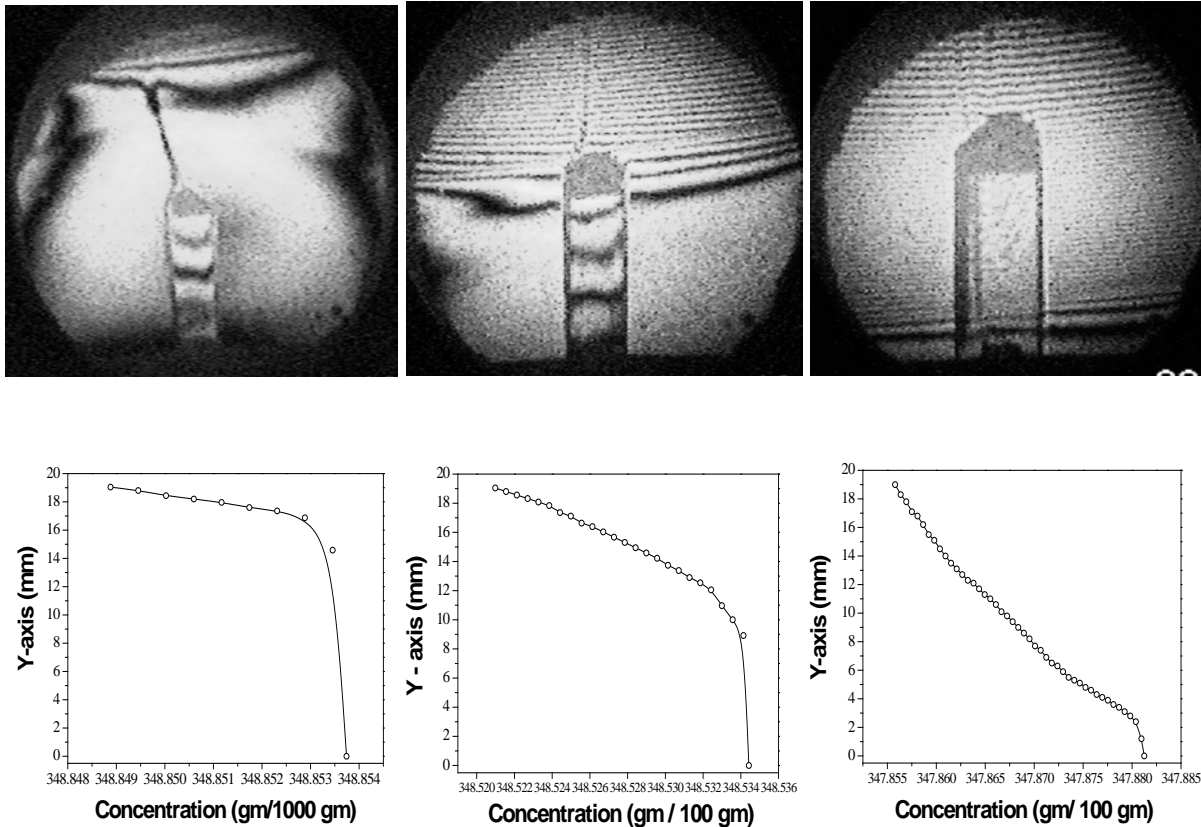
Figure 15: First row - Infinite fringe interferograms of concentration gradient inside the growth chamber at three stages of growth under conditions of free convection. Second row - the computed concentration distribution corresponding to the images in the top row are shown. As the solute-depleted solution accumulates in the upper region of the crystallizer, the concentration diminishes locally, producing a density stratified, gravitationally stable configuration. The Mach-Zehnder interferometer proves to be a very sensitive diagnostic to detect and quantify solution stratification during the crystallization process, a stage that is detrimental for growth of good quality crystals. Images adapted from *Imaging transport phenomena and surface micromorphology in crystal growth using optical techniques*, Sunil Verma and K. Muralidhar, Nat. Acad. Sci. Letts. 33 (2010) 107-121.
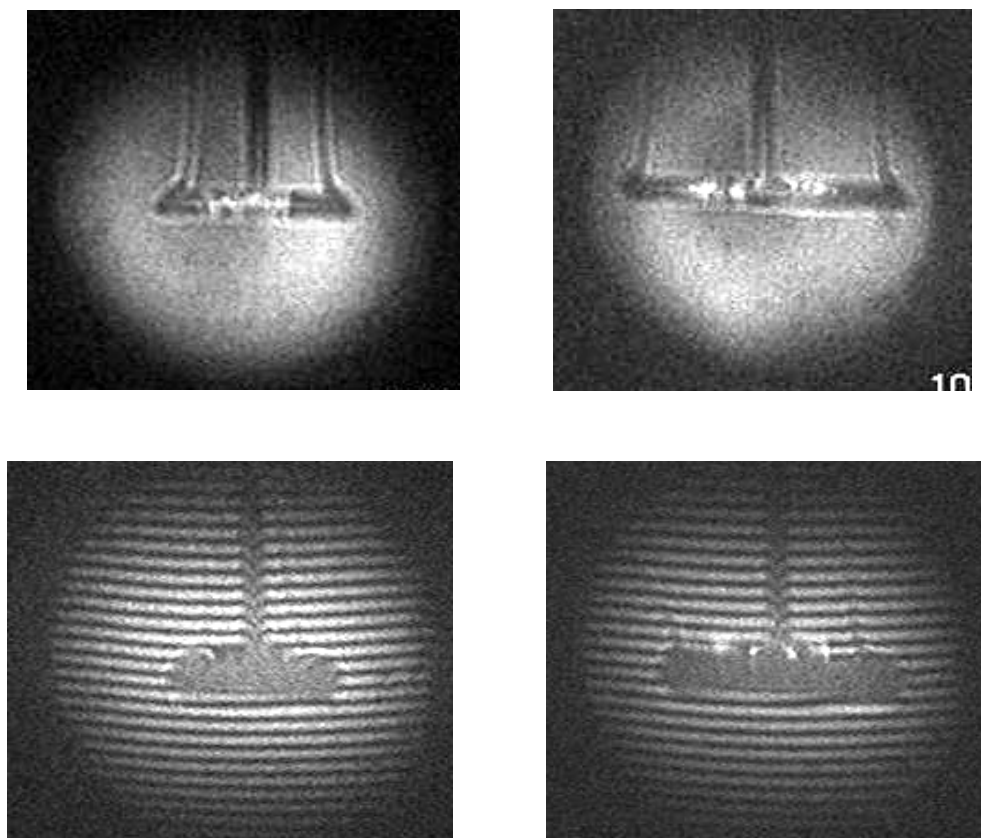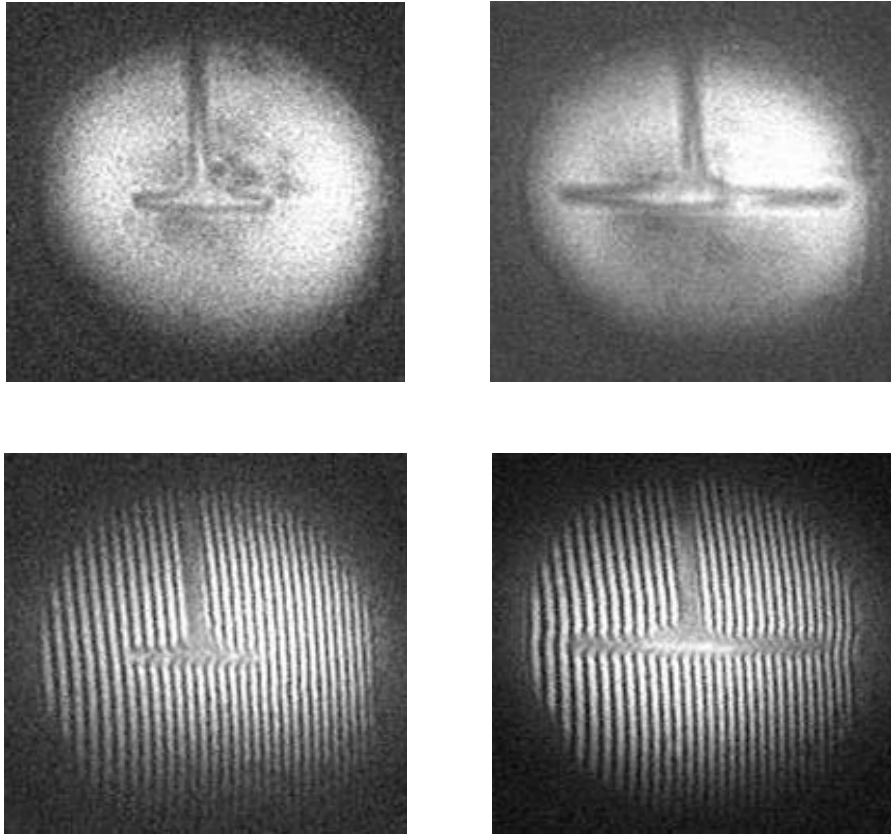
Figure 16: First row - Infinite fringe interferograms of a crystal growing under free convection conditions in the top hanging geometry. . The free convection plume and the diffusion boundary layer are clearly visible. Second row - Wedge fringe interferograms of a crystal growing under free convection conditions in the top hanging geometry. The diffusion boundary layer is not visible as clearly as is in case of infinite fringe interferogram. Images adapted from *Convection, concentration, and surface features analysis during crystal growth from solution using optical diagnostics,* Sunil Verma and K. Muralidhar, in Recent Research Developments in Crystal Growth, Vol. 5, Transworld Research Network, India, 2009, pp. 141-314.
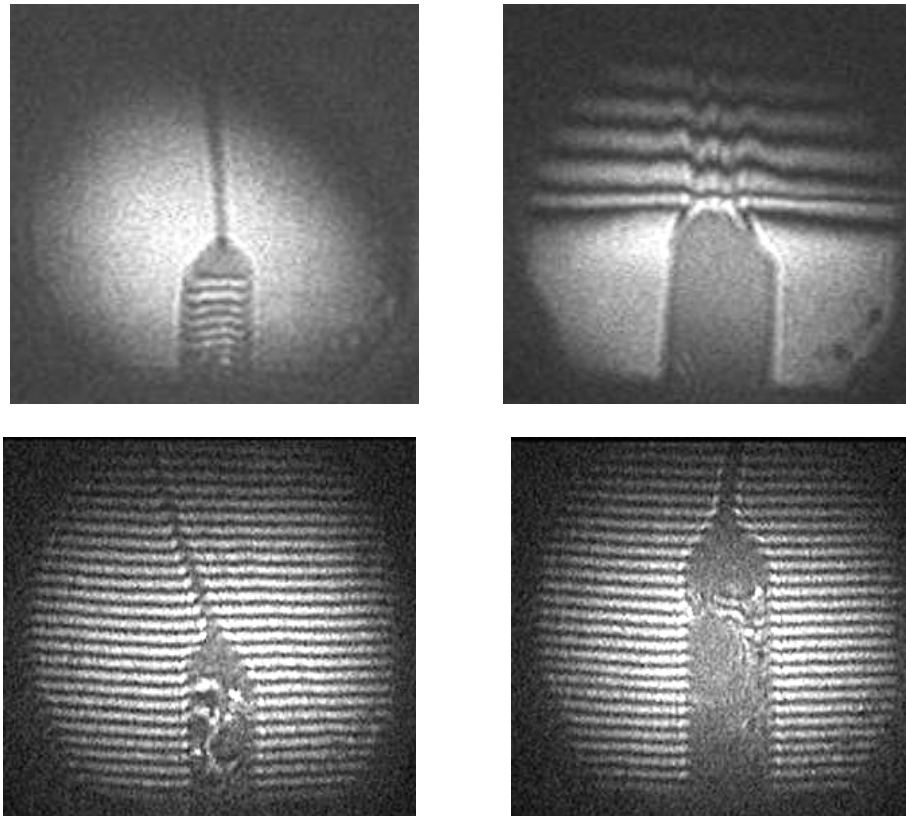
Figure 17: First row - Infinite fringe interferograms of a crystal growing under forced convection conditions in the top hanging geometry. Second row - Wedge fringe interferograms of a crystal growing under forced convection conditions in the top hanging geometry. No buoyancy driven convection plumes are visible. Minor fringe distortion is visible near to the crystal-solution interface. Images adapted from *Convection, concentration, and surface features analysis during crystal growth from solution using optical diagnostics,* Sunil Verma and K. Muralidhar in Recent Research Developments in Crystal Growth, Vol. 5, Transworld Research Network, India, 2009, pp. 141-314.

Figure 18: First row - Infinite fringe interferograms of the crystal growing on a platform under free convection conditions. The concentration gradient is clearly visible in the second image. Second row - Wedge fringe interferograms of crystal growing under free convection conditions in a platform geometry. The free convection plume and the diffusion boundary layers are visible in the infinite as well as wedge fringe interferograms. Images adapted from: *Convection, concentration, and surface features analysis during crystal growth from solution using optical diagnostics,* Sunil Verma and K. Muralidhar, Recent Research Developments in Crystal Growth, Vol. 5, Transworld Research Network, India, 2009, pp. 141-314.
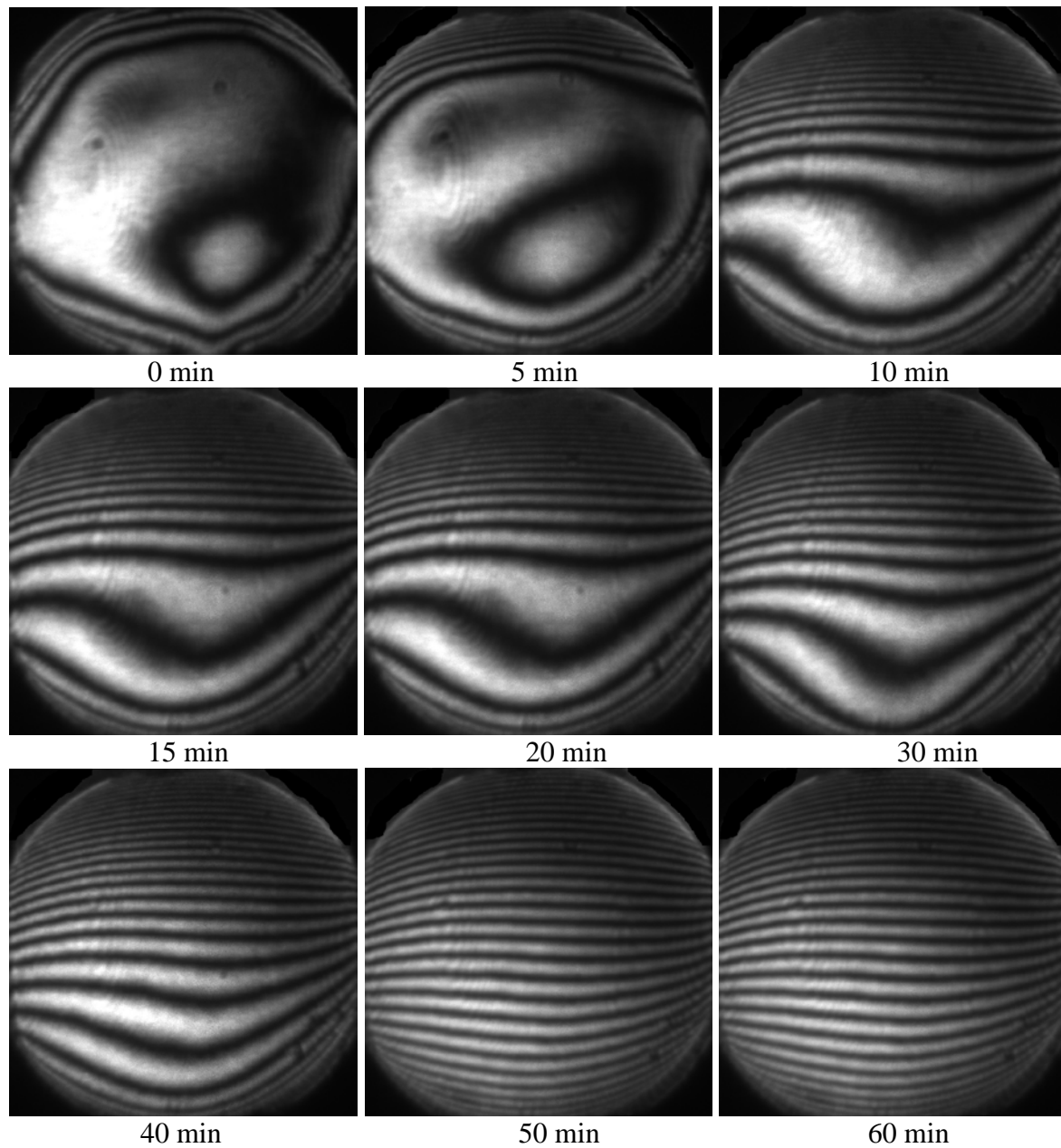
Figure 19: Heat conduction in a differentially heated layer of water with the top surface maintained at 23°C and the lower surface at 18°C. The thermal field is images using a Mach-Zehnder interferometer in the infinite fringe setting. Images adapted from M.Tech. dissertation of Vishnu Singh, Indian Institute of Technology, Kanpur (2009).
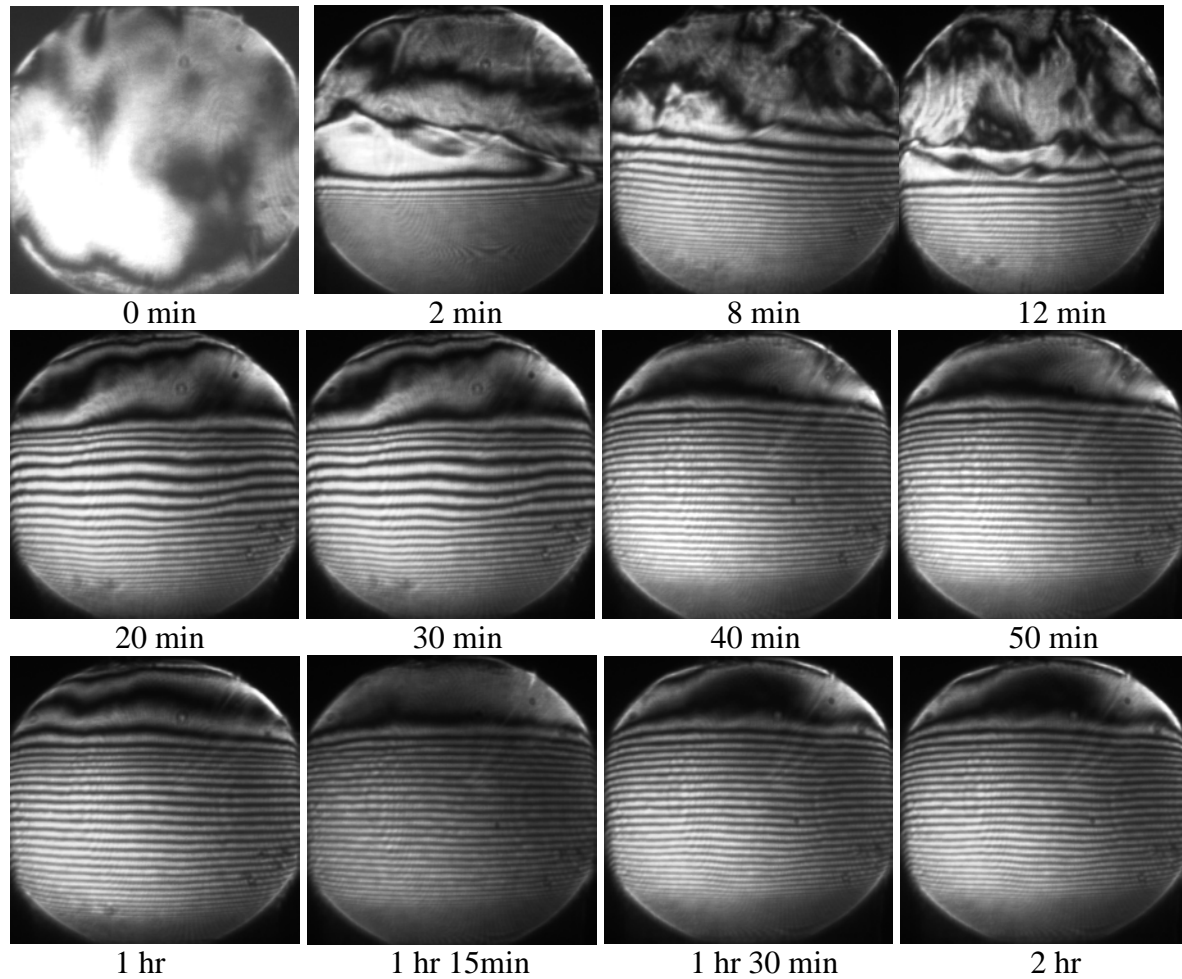
Figure 20: A layer of sugar applied at the base slowly dissolves in water. The concentration of sugar in water changes with time. It is accompanied by the appearance of interferometric fringes. Images adapted from doctoral dissertation of Susheel Bhandari, Indian Institute of Technology, Kanpur (2009).
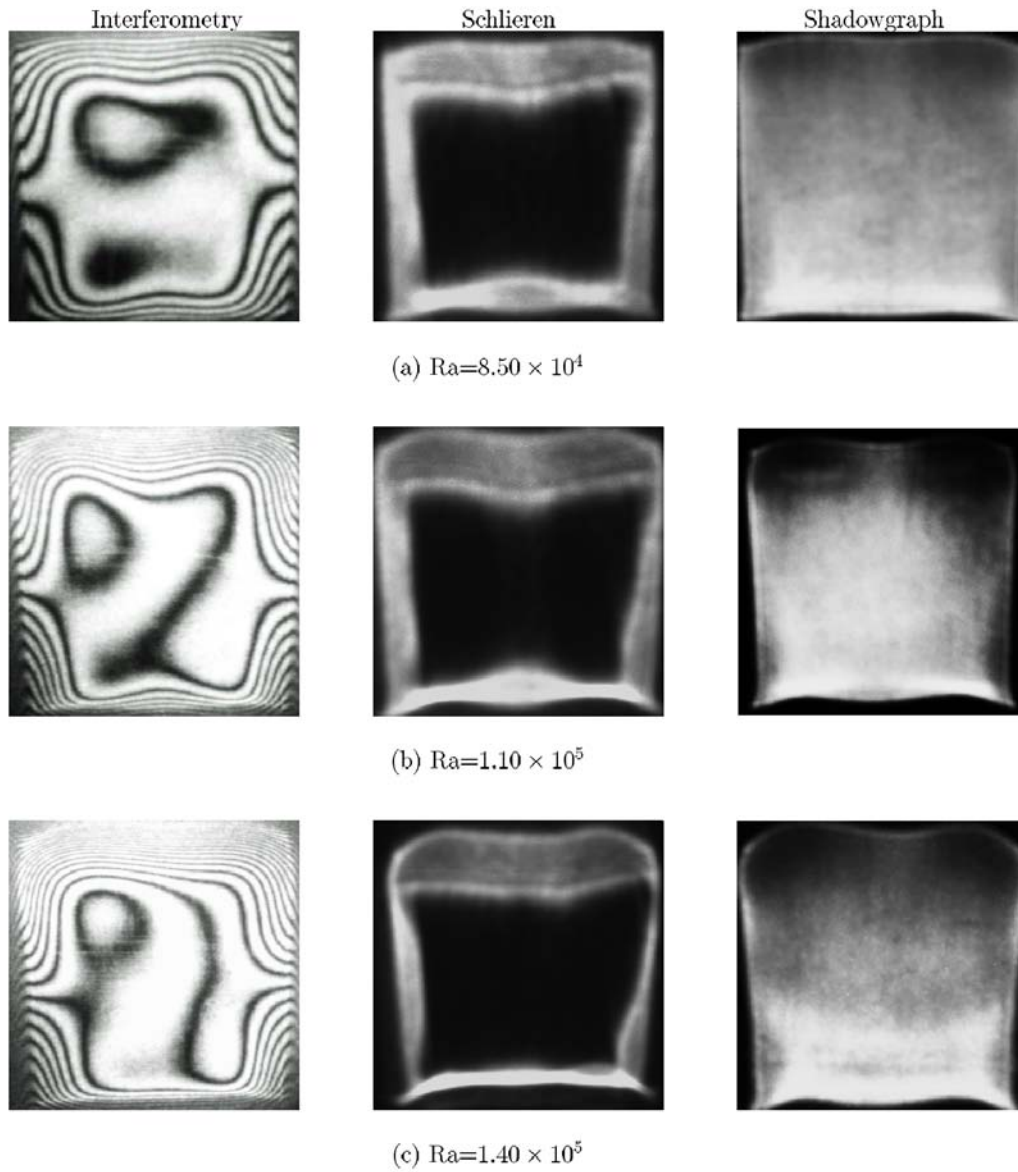
| Interferometry | Schlieren | Shadowgraph |

(a) Ra=8.50×10^4

(b) Ra=1.10×10^5

(c) Ra=1.40×10^5

Figure 21: Natural convection in a rectangular cavity of square cross-section. The fluid medium in the cavity is air and convection is driven by the temperature differential between a hot lower wall and a cold upper wall. The side walls are insulated. The symbol Ra is Rayleigh number and is a measure of the strength of natural convection in the cavity. The first column carries interferometric fringes. The second and third columns contain a re-distribution of light intensity as obtained from schlieren and shadowgraph techniques. Images adapted from *Optical imaging and control of convection around a crystal growing from its aqueous solution,* K. Muralidhar, Atul Srivastava and P.K. Panigrahi, in New Developments in Crystal Growth Research, Nova Publishers, 2005, pp. 1-89.
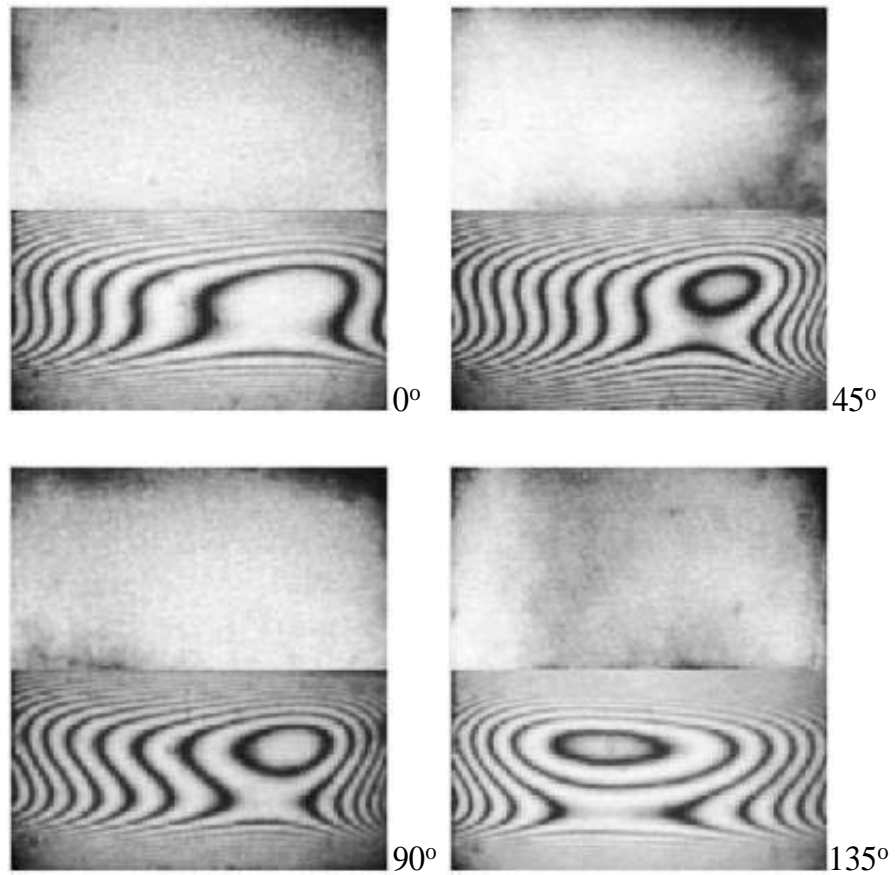
Figure 22: Buoyancy driven convection in an octagonal cavity half-filled with 50 cSt silicone oil, the rest being air. The lower surface is heated while the top surface is cooled. The figure shows interferometric projections when the thermal field is viewed in various directions – 0, 45, 90, and 135°. Images adapted from *Interferometric study of convection in superposed gas-liquid layers,* Sunil Punjabi, Doctoral dissertation, Indian Institute of Technology, Kanpur (2002).
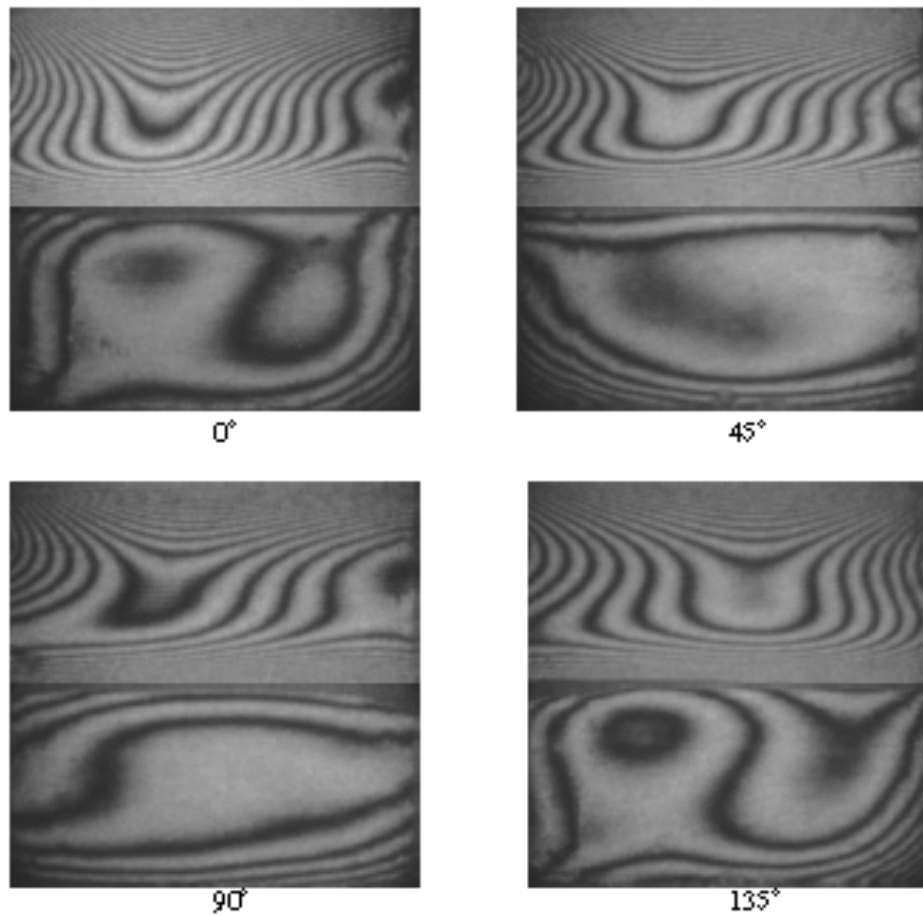
Figure 23: Long-time interferograms formed in an octagonal cavity containing silicone oil (50 cSt) floating over water as recorded from four different angles; Overall temperature difference is 1.8 K, the top plate being cooler than the one at the base. Of special interest are the energy and momentum transfer at the oil-water interface. Images adapted from *Buoyancy-driven convection in two superposed fluid layers in an octagonal cavity,* Sunil Punjabi, K. Muralidhar and P.K. Panigrahi, International Journal of Thermal Sciences, 43 (2004) 849-864.
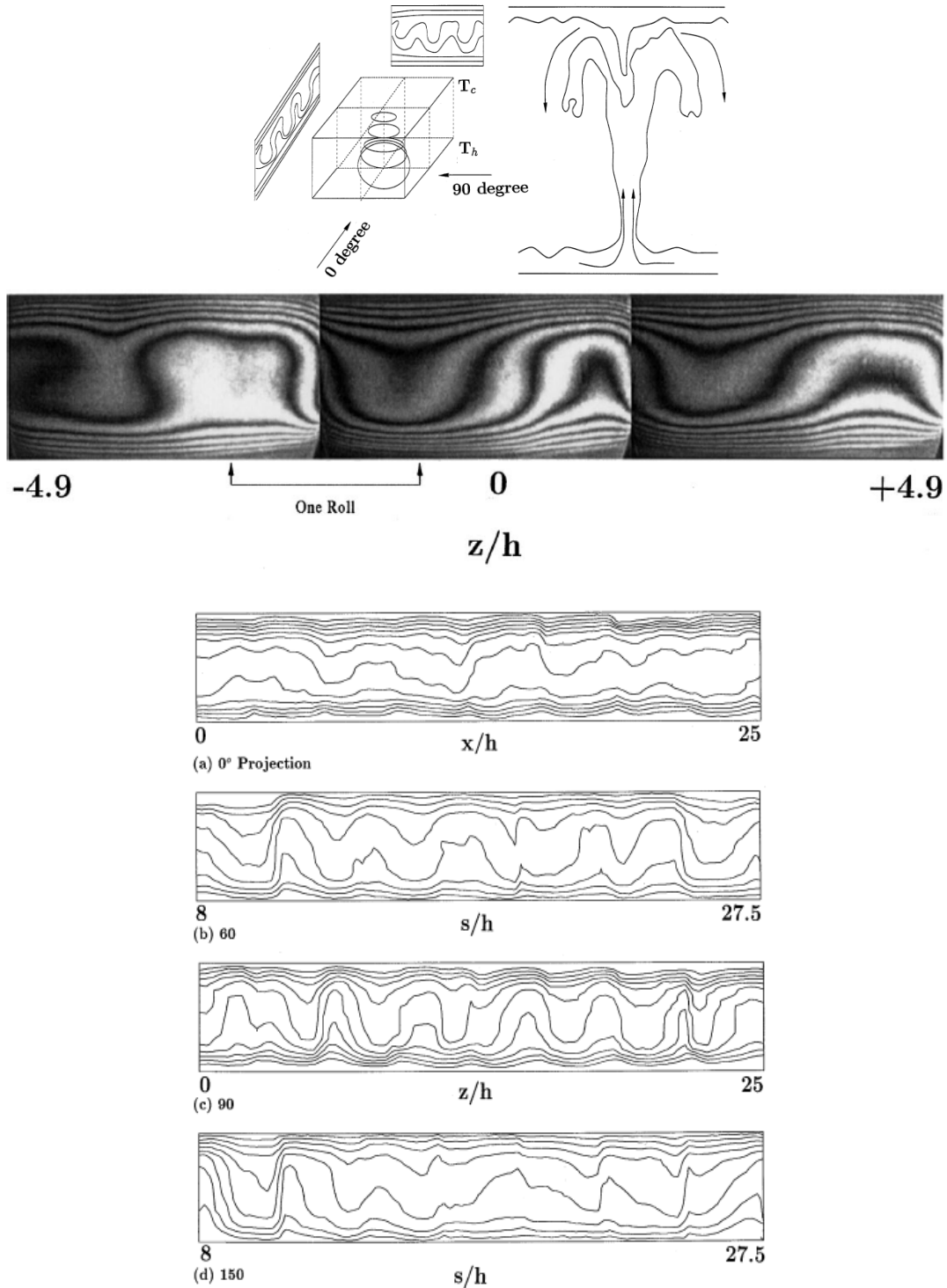
Figure 24: Buoyancy-driven convection in a differentially heated cavity. The roll patterns of the flow field are seen as fringe displacement in the interferograms. The flow pattern is three dimensional and sketched at the top of the figure. The corresponding interferograms seen from various viewing directions are shown below. Images adapted from *Experimental study of Rayleigh-Benard convection using interferometric tomography,* Debasish Mishra, Doctoral dissertation, Indian Institute of Technology, Kanpur (1998).
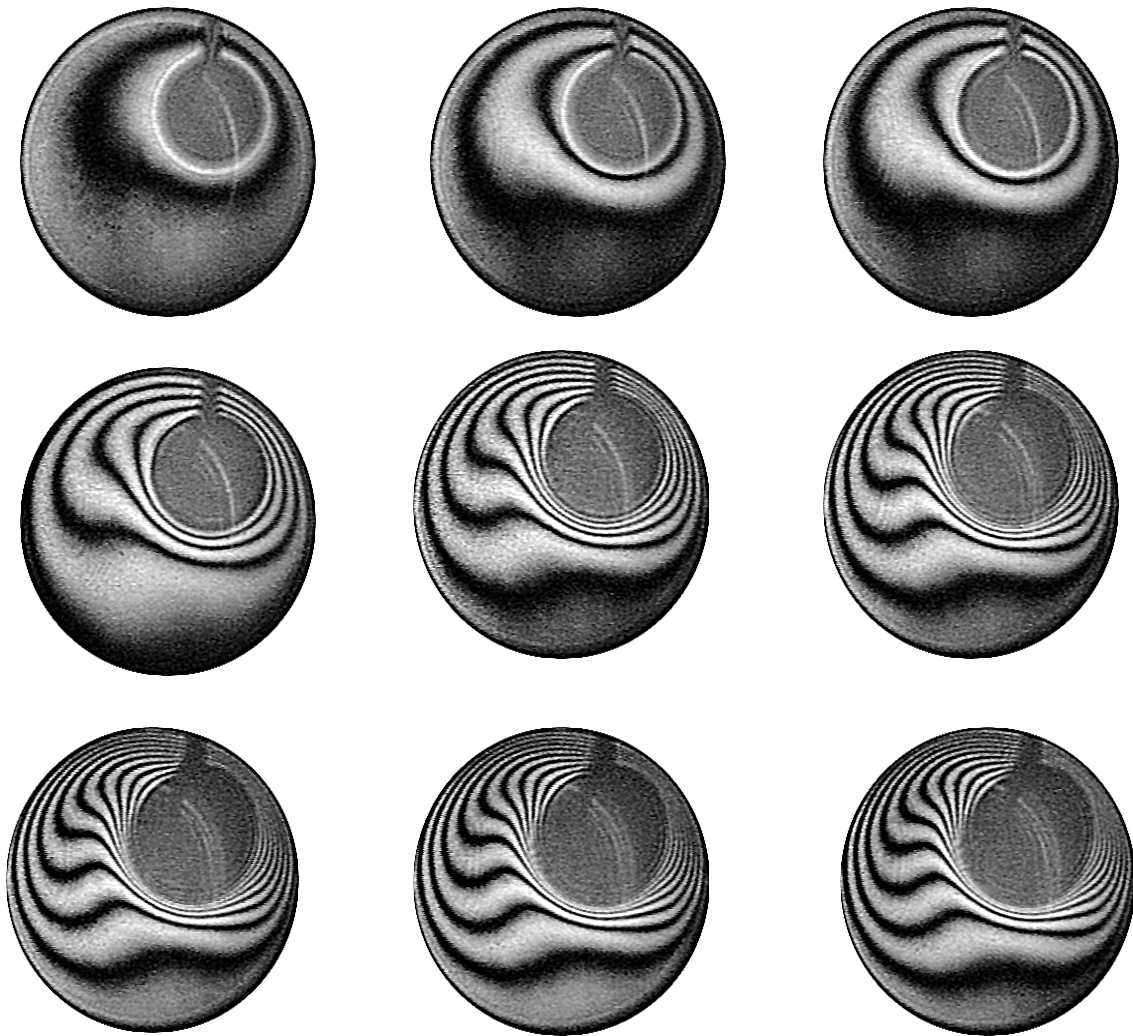
Figure 25: Interferograms recorded in an eccentric annulus with the gap filled with air. The inner cylinder is heated while the outer cylinder is cooled. The images show a time sequence of interferograms from the initial infinite fringe setting all the way till steady state is reached. Images adapted from *Interferometric study of steady and unsteady convection in cylindrical and eccentric annuli,* Manoj Ranjan, M.Tech. dissertation, Indian Institute of Technology, Kanpur, (2005).
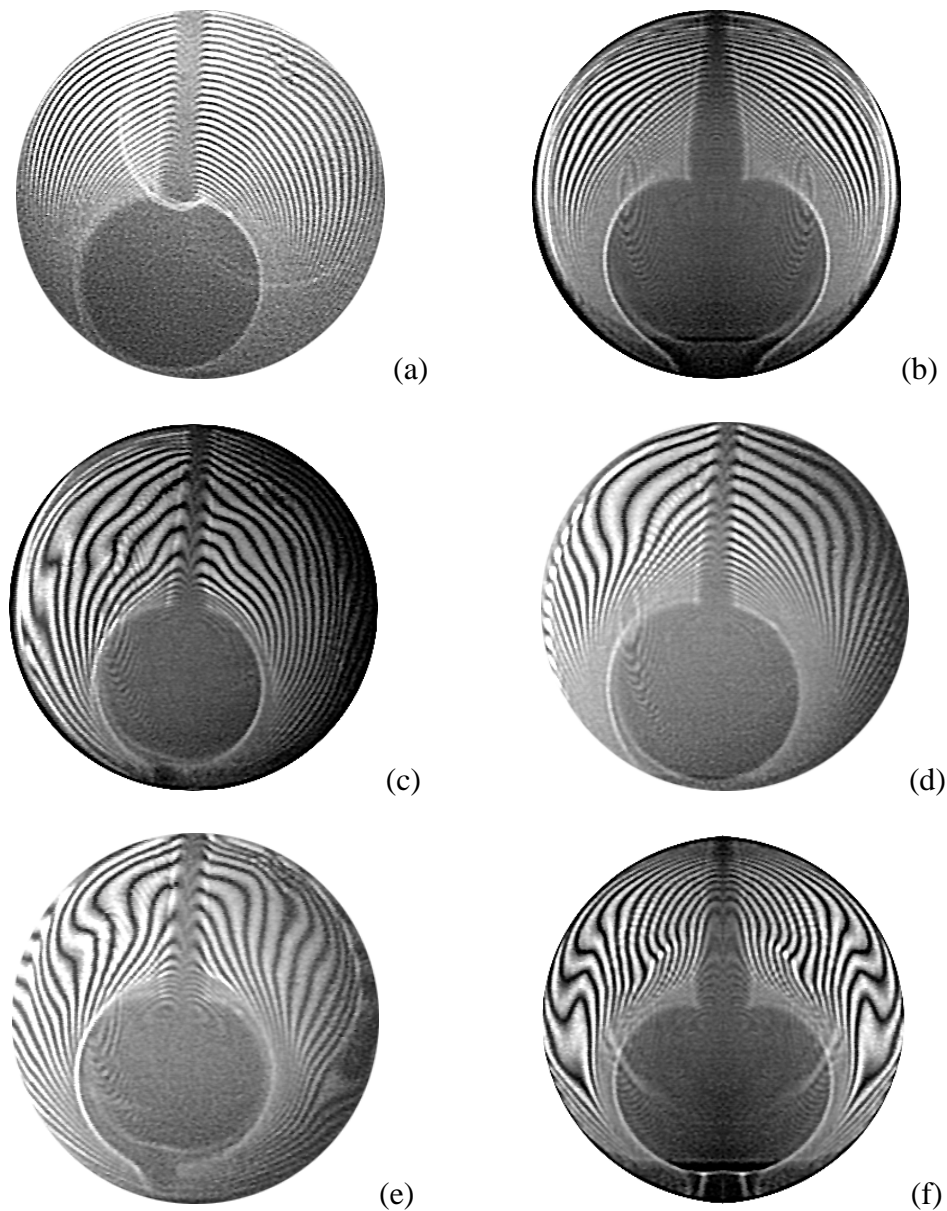
Figure 26: Interferograms recorded during heat transfer in an eccentric annulus when the gap is filed with 50 cSt silicone oil. The applied temperature differences increase from (a) to (e) from 0.2 to 2 K. When compared to air, the principal differences observed in the fringe patterns are an increase in the number of fringes, strong refraction errors near the inner cylinder, symmetric thermal fields about the position of the inner cylinder and weak convection effects. Images adapted from *Interferometric study of steady and unsteady convection in cylindrical and eccentric annuli,* Manoj Ranjan, M.Tech. dissertation, Indian Institute of Technology, Kanpur, (2005).
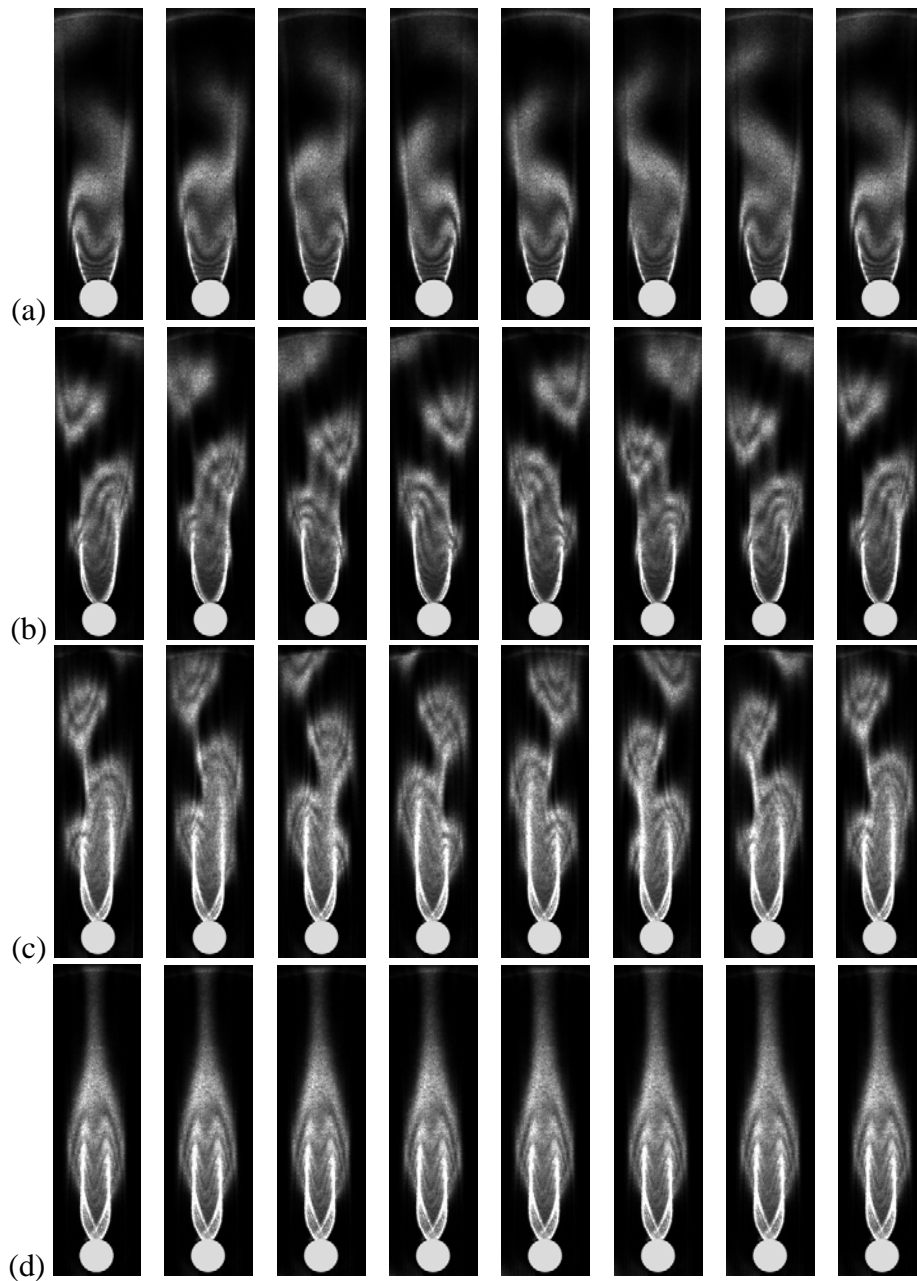
Figure 27: Instantaneous schlieren images (a-e) for flow past a circular cylinder separated by a time interval of one eighth of the time period of vortex shedding at Re=110. (a) Ri=0.052, (b) Ri=0.104, (c) Ri=0.140, and (d) Ri=0.157. For Ri≥0.157, images show steady patterns. Images adapted from *Effect of buoyancy on the wakes of circular and square cylinders - a schlieren-interferometric study,* S.K. Singh, P.K. Panigrahi and K. Muralidhar, Experiments in Fluids, 43 (2007) 101-123.

3. CONCLUSION

The present chapter provides an introduction to the subject of interferometry as a method of measurement of temperature in fluids and solute concentration in liquids. As a rule, a coherent source of light such as a laser is required and the medium is transparent and non-scattering. The record originates in refractive index variations and is an image of the density field in the form of fringes. The data contains information related to the line-of-sight averaged density and hence temperature as well as concentration. Specific advantages of the interferometer can be listed as follows:

i. The measurement takes place for the entire cross-section and as opposed to point measurements, it classifies as a field scale technique.

ii. Data is localized at the fringes. Thus, temperature and concentration are available at all points along a fringe. In practice, the resolution is limited by the number of pixels available in the camera.

iii. The measurement is instantaneous without any time lag. In experiments, temporal resolution is limited by that of the camera.

iv. An image, namely the interferogram is a two dimensional projection of the material density distribution. However, information in three dimensions can be recovered by reconfiguring the interferometer for holography or analytically using the principles of tomography.

v. A variety of optical configurations are available. These can be used to adjust the sensitivity of the measurement. Alternatives such as isotherms, profiles, and gradients can be explored for the image content.

vi. The breadth of applications reported in this chapter shows that interferometry can play an important role in industrial processes and applications.

Interferometry may be limited by the need for frequent alignment and a controlled atmosphere. Ideally, the optics should be computer controlled. A compensation chamber may be required for sensitive measurements. The presence of a solid phase such as particulates will result in scattering and diminish the utility of interferometry. These subjects form the focus of future research.

ACKNOWLEDGEMENT

NOMENCLATURE

T_{supersat}	Supersaturated (or growth) temperature
T_{sat}	Saturation temperature
$\varDelta T = T_{\text{supersat}} - T_{\text{sat}}$	Supercooling
C_{supersat}	Supersaturated concentration
C_{sat}	Saturated concentration
$\varDelta C = C_{\text{supersat}} - C_{\text{sat}}$	Driving force for crystal growth (concentration is expressed in units of grams of solute per 1000 gm of solvent)
$\sigma = \dfrac{C_{\text{supersat}} - C_{\text{sat}}}{C_{\text{sat}}}$	Relative supersaturation
NLO	Non-linear optics
KDP	Potassium Dihydrogen Phosphate
I_s	Intensity on screen in the presence of disturbance
I_o	Intensity on screen in the absence of disturbance
n	Refractive index of the solution
λ	Wavelength of the laser light
t	Thickness of film
θ	Angle of incidence
r	Radius of the cluster
$\theta_{sol}, \theta_{qtz}, \theta_{air}$	Angle of incidence of the light at the quartz window, the angle of refraction of the light ray into the quartz window, the angle of refraction of the light ray in the air, respectively
$n_{sol}, n_{qtz}, n_{air}$	Refractive index of the KDP solution, the refractive index of the quartz window and the refractive index of the quartz window
$Gr = \rho \dfrac{\partial \rho}{\partial C} \dfrac{(C_o - C_i)}{\mu^2} g\, L^3$	Grashof number
$\text{Re} = \dfrac{\omega L^2}{\nu}$	Reynolds number
$Sc = \dfrac{\mu}{\rho D}$	Schmidt number

ρ	Density of the solution at a certain temperature in kg/m^3
$\partial\rho/\partial C$	Gradient of density with concentration
C_o	Bulk solute concentration in mole/m^3
C_i	Interface concentration near to the crystal
g	Acceleration due to gravity in m/s^2
L	Characteristic length in m
D	Diffusion coefficient of solute in the solution in m^2/s
k	Gladstone-Dale constant
ΔC_E	Concentration change per fringe shift

REFERENCES

[Bedarida, 1977] F. Bedarida, L. Zefiro and C. Pontiggia, Holographic control of diffusion coefficients in water solutions: Crystal growth from solutions, in: "Applications of Holography and Optical Data Processing", E. Marom and A. A. Friesem (Eds), (Pergamon Press, Oxford, 1977), pp. 259-265.

[Bedarida, 1992] F. Bedarida, G.A. Dall'Aglio, L. Gatti and F. Solitro, The sensitivity of an optical fiber holographic interferometer, Proc. 8th Euro. Symp. on Materials and Fluid Sciences in Microgravity, Brussels, Belgium, ESA SP-333 (August 1992), 321-323.

[Bhandari, 2009] Susheel Bhandari, Doctoral dissertation, Indian Institute of Technology, Kanpur, India (2009).

[Bruning, 1974] J.H. Bruning, D.R. Herriott, J.E. Gallagher, D.P. Rosenfeld, A.D. White and D.J. Brangaccio, Digital wavefront measuring interferometer for testing optical surfaces and lenses, Appl. Opt., 13 (11) (1974) 2693-2703.

[Bunn, 1949] C.W. Bunn, Crystal growth from solution. II. Concentration gradients and the rates of growth of crystals, Discuss. Faraday Society, 5 (1949) 132-144.

[Censor, 1983] Y. Censor, Finite series-expansion reconstruction methods, Proc. IEEE, 71 (3) (1983) 409-419.

[Chen, 1977] P.S. Chen, Convection irregularities during solution growth and relation to crystal-defect formation, Ph.D. dissertation, Univ. of Southern California, Los Angeles, CA, USA, (1977), 213 pp.

[Chen, 1979A] P.S. Chen, W.R. Wilcox and P.J. Shlichta, Free convection about a rectangular prismatic crystal growing from a solution, Int. J. Heat Mass Transfer, 22 (1979) 1669-1679.

[Chen, 1979B] P.S. Chen, P.J. Shlichta, W.R. Wilcox and R.A. Lefever, Convection phenomena during the growth of sodium chlorate crystals from solution, J. Cryst. Growth, 47 (1979) 43-60.

[Chen, 2002] W.C. Chen, D.D. Liu, W.Y. Ma, A.Y. Xie and J. Fang, The determination of solute distribution during growth and dissolution of $NaClO_3$ crystals: the growth of large crystals, J. Cryst. Growth, 236 (2002) 413-419.

[Cloud, 1995] Gary Cloud (with contributions from K. Creath), Phase shifting to improve interferometry, Chapter 22, in: "Optical Methods of Engineering Analysis", Gary Cloud, (Cambridge University Press, 1995), pp. 477-491.

[Cole, 1995] T. Cole, A. Kathman, S. Koszelak, and A. McPherson, Determination of local refractive index for protein and virus crystals in solution by Mach-Zehnder interferometry, Analytical Biochem., 231 (1995) 92-98.

[Collier, 1971] R.J. Collier, C.B. Burckhardt and L.H. Lin, "Optical Holography", (Academic Press, New York, 1971), 605 pp.

[Creath, 1986] K. Creath, Comparison of phase-measurement algorithms, SPIE 680 (1986) 19-28.

[Creath, 1987] K. Creath, WYKO systems for optical metrology, SPIE 816 (1987) 111-126.

[Creath, 1988] K. Creath, Phase-measurement interferometric techniques, Chapter V, in: "Progress in Optics", Vol. XXVI, E. Wolf (Ed.), (Elsevier Science Publishers B.V., Netherlands, 1988), pp. 349-393.

[Dainty, 1984] J.C. Dainty (Ed.), "Laser Speckle and Related Phenomena", 2nd ed., (Springer-Verlag, Berlin, 1984), 342 pp.

[Dinakaran, 2010] S. Dinakaran, Sunil Verma, S. Jerome Das, S. Kar and K.S. Bartwal, Optical imaging of the growth kinetics and polar morphology of zinc tris (thiourea) sulphate (ZTS) single crystals, Cryst. Res. Technol. 45 (3) (2010) 233-238

[Duan, 2001] L. Duan and J. Z. Shu, The convection during $NaClO_3$ crystal growth observed by the phase shift interferometer, J. Cryst. Growth, 223 (2001) 181-188.

[Dubois, 1999] F. Dubois, L. Joannes, O. Dupont, J.L. Dewndel and J.C. Legros, An integrated optical set-up for fluid-physics experiments under microgravity conditions, Meas. Sci. Technol., 10 (1999) 934-945.

[Ducruix, 1992] A. Ducruix and R. Giege, Crystallization of Nucleic Acids and Proteins, (Oxford Univ. Press, 1992), 331 pp.

[Dupont, 1995] O. Dupont, J.L. Dewandel and J.C. Legros, Use of electronic speckle pattern interferometry for temperature distribution measurements through liquids, Opt. Letts., 20 (1995) 1824-1826.

[Ecker, 1987] A. Ecker, Solidification front dynamics examined by holographic interferometric measurement of temperature and concentration using transparent model systems, Final Report, NASA (March, 1987).

[Ecker, 1988] A. Ecker, Two-wavelength holographic measurement of temperature and concentration during alloy solidification, J. Thermophys. Heat Transfer, 2(3) (1988) 193-196.

[El-Wakil, 1964] M.M. El-Wakil and C.L. Jaeck, A two-wavelength interferometer for the study of heat and mass transfer, J. Heat Transfer, 79 (1964) 464-466.

[Gabor, 1948] D. Gabor, A new microscopic principle, Nature, 161 (1948) 777.

[Gabor, 1949] D. Gabor, Microscopy by reconstructed wavefronts, Proc. Soc. Roy., A197 (1949) 457-484.

[Gatti, 1989] L. Gatti, F. Solitro, F. Bedarida, P. Boccacci, G.A. Dall'Aglio and L. Zefiro, Three-dimensional measurements of concentration fields in crystal growth by multidirectional holographic interferometry, SPIE 1162 (1989) 126-131.

[Goldstein, 1996] R.J. Goldstein and T.H. Kuehn, Optical Systems for Flow Measurement: Shadowgraph, Schlieren, and Intreferometric Techniques, in: "Fluid Mechanics Measurements", R. J. Goldstein (Ed.), (Taylor & Francis, New York, 1996), pp. 451-508.

[Greivenkamp, 1992] J.E. Greivenkamp and J.H. Bruning, Phase shifting interferometry, Chapter 14, in: "Optical Shop Testing", 2nd Ed., Daniel Malacara (Ed.), (John Wiley & Sons, Inc., New York, 1992), pp. 501-598.

[Gull, 1986] S.F. Gull and T.J. Newton, Maximum entropy methods, Appl. Opt., 25 (1986) 156-160.

[Hariharan, 1985] P. Hariharan, "Optical Interferometry", (Academic Press, Sydney, 1985), 303 pp.

[Hariharan, 1986] P. Hariharan, "Optical Holography: Principles, Techniques and Applications", (Cambridge University Press, Cambridge, 1986), 319 pp.

[Hariharan, 2002] P. Hariharan, "Basics of Holography", (Cambridge University Press, Cambridge, 2002), 161 pp.

[Heffinger, 1966] L.O. Heffinger, R.F. Wuerker and R.E. Brooks, Holographic interferometry, J. Appl. Phys., 37 (1966) 642-649.

[Herman, 1980] G.T. Herman, "Image Reconstruction from Projections: The Fundamentals of Computerized Tomography", (Academic Press, New York, 1980), 316 pp.

[Jones, 1989] R. Jones and C. Wykes, "Holographic and Speckle Interferometry", 2nd Ed., (Cambridge University Press, 1989), p. 368.

[Kang, 2001] Q. Kang, L. Duan and W.R. Hu, Mass transfer process during the NaClO3 crystal growth process, Int. J. Heat and Mass Transfer, 44 (2001) 3213-3222.

[Kim, 1998A] Y.K. Kim, B.R. Reddy and R.B. Lal, Laser and Mach-Zehnder interferometer for in-situ monitoring of crystal growth and concentration variation, SPIE 3479 (1998) 172-180.

[Kumar, 2008] N.V.N. Ravi Kumar, K. Muralidhar, and Y.M. Joshi, On refractive index of ageing suspensions of laponite, Applied Clay Science, 42 (2008) 326-330.

[Lenski, 1991] H. Lenski and M. Braun, Laser beam deflection: a method to investigate convection in vapor growth experiments, SPIE 1557, "Crystal Growth in Space and Related Optical Diagnostics", James D. Trolinger, Ravindra B. Lal (Eds.), (1991) 124-131.

[Lewitt, 1983] R.M. Lewitt, Reconstruction algorithms: Transform methods, Proc. IEEE, 71 (3) (1983) 390-408.

[Lokberg, 1980] O.J. Lokberg, Electronic speckle pattern interferometry, Phys. Technol., 11 (1980) 16-22.

[Maruyama, 1999] S. Maruyama, T. Shibata and K. Tsukamoto, Measurement of diffusion fields of solutions using real-time phase-shift interferometer and rapid heat-transfer control system, Exp. Therm. Fluid Sci., 19 (1999) 34-48.

[Maruyama, 2002] S. Maruyama, K. Ohno, A. Komiya and S. Sakai, Description of the adhesive crystal growth under normal and micro-gravity conditions employing experimental and numerical approaches, J. Cryst. Growth, 245 (2002) 278-288.

[Mayinger, 1993] F. Mayinger, Image-forming optical techniques in heat transfer: revival by computer-aided data processing, Trans. ASME, 115 (1993) 824-834.

[Mayinger, 1994] F. Mayinger (Ed.), "Optical Measurements: Techniques and Applications", (Springer-Verlag, Berlin, 1994), 463 pp.

[McPherson, 1982] A. McPherson, "Preparation and Ansalysis of Protein Crystals", (Wiley, New York, 1982), 371 pp.

[McPherson, 1999] A. McPherson, A.J. Malkin, Y.G. Kuznetsov, S. Koszelak, M. Wells, G. Jenkins, J. Howard and G. Lawson, The effects of microgravity on protein crystallization:

Evidence for concentration gradients around growing crystals, J. Crystal Growth, 196 (1999) 572-586.

[McPherson, 2001] A. McPherson, "Crystallization of Biological Macromolecules", 2nd ed., (Cold Spring Harbor Laboratory Press, 2001) 586 pgs. (1st ed. 1998).

[Mehta, 1990] J.M. Mehta, Dual wavelength interferometric technique for simultaneous temperature and concentration measurement in liquids, Appl. Opt., 29 (13) (1990) 1924-1932.

[Merzkirch, 1974] W.F. Merzkirch, "Flow Visualization", (Academic Press, New York, 1974), 250 pp.

[Merzkirch, 1987] W.F. Merzkirch, "Flow Visualization", 2nd Edition, (Academic Press, New York, 1987), 260 pp.

[Mishra, 1998] Debasish Mishra, Experimental Study of Rayleigh Benard Convection using Interferometric Tomography, Ph.D. dissertation, Indian Institute of Technology, Kanpur, India (1998).

[Mishra, 1999] Debasish Mishra, K. Muralidhar and P. Munshi, Interferometric study of Rayleigh-Benard convection using tomography with limited projection data, Numerical Heat Transfer, 12 (1999) 117-136.

[Mullin, 2001] J.W. Mullin, Crystallization, 4th ed., (Butterworth-Heinemann, Oxford, 2001).

[Muralidhar, 2001] K. Muralidhar, Temperature field measurement in buoyancy-driven flows using interferometric tomography, Ann. Rev. Heat Transf., 12 (2001) 265-375.

[Muralidhar, 2005] K. Muralidhar, Atul Srivastava and P.K. Panigrahi, Optical imaging and control of convection around a crystal growing from its aqueous solution, in New Developments in Crystal Growth Research (Nova Publishers, New York, 2005) pp. 1-89.

[Murphy, 1971] C.G. Murphy and S.S. Alpert, Dependence of refractive index temperature coefficients on the thermal expansivity of liquids, Am. J. Phys., 39 (7) (1971) 834-836.

[Nagashima, 2000] K. Nagashima and Y. Furukawa, Time development of a solute diffusion field and morphological instability on a planar interface in the directional growth of ice crystals, J. Cryst. Growth, 209 (2000) 167-174.

[Nakadate, 1990] S. Nakadate and I. Yamaguchi, Japanese patent describing the technique of real-time phase shifting interferometry, Japanese Patent # H02-287107 (1990).

[Nakadate, 1995] S. Nakadate, Real-time fringe pattern processing and its applications, SPIE 2544 (1995) 74-86.

[Natterer, 2001] F. Natterer, "The Mathematics of Computerized Tomography", (Philadelphia, PA, SIAM 2001), 222 pp.

[Onuma, 1988] K. Onuma, K. Tuskamoto and I. Sunagawa, Role of buoyancy driven convection in aqueous soultion; A case study of $Ba(NO_3)_2$ crystal, J. Cryst. Growth, 89 (1988) 177-188.

[Onuma, 1989] K. Onuma, K. Tuskamoto and I. Sunagawa, Measurement of surface supersaturations around a gowing K-alum crystal in aqueous solution, J. Cryst. Growth, 98 (3) (1989) 377-383.

[Onuma, 1993] K. Onuma, K. Tsukamoto and S. Nakadate, Application of real time phase shift interferometer to the measurement of concentration field, J. Cryst. Growth, 129 (1993) 706-718.

[Owen, 1975] W.A. Owen et al. Advanced Application Flight Experiment: Effect of Residual and Transient Convection on Crystallization in a Spaceflight Environment, Semiannual Report, NASA Code. No. 638-10-00-01-00 (Jet Propulsion Laboratory, Pasadena, CA, USA, March 1975; see also later reports November 1975 and June 1976.

[Owen, 1982] R.B. Owen, Interferometry and holography in a low-gravity environment, Appl. Opt., 21 (8) (1982) 1349-1355.

[Owen, 1986] R.B. Owen, R.L. Kroes and W.K. Witherow, Results and further experiments using Spacelab holography, Opt. Lett., 11 (7) (1986) 407-409.

[Paschotta, 2008] Rüdiger Paschotta, Encyclopedia of Laser Physics and Technology (Wiley-VCH, Berlin, 2008) 844 pp.

[Piano, 2000] E. Piano, G.A. Dall'Aglio, S. Crivello, R. Chittofrati and F. Puppo, New optical techniques for crystal growth from fluids, Materials Chem. Phys., 66 (2000) 266-269.

[Piano, 2001] E. Piano, G.A. Dall'Aglio, R. Chittofrati, S. Crivello and F. Puppo, A non-destructive interferometric technique for analysis of crystal growth and fluid dynamics, Ann. Chim. Sci. Mat., 26 (2001) 23-28.

[Pletser, 2001] V. Pletser, O. Minster, R. Bosch, L. Potthast and J. Stapelmann, The protein crystallisation diagnostics facility: status of the ESA programme on the fundamentals of protein crystal growth, J. Cryst. Growth, 232 (2001) 439-449.

[Punjabi, 2002] Sunil Punjabi, Interferometric study of convection in superposed gas-liquid layers, Doctoral dissertation, Indian Institute of Technology, Kanpur, India (2002).

[Punjabi, 2004] Sunil Punjabi, K. Muralidhar and P.K. Panigrahi, Buoyancy-driven convection in two superposed fluid layers in an octagonal cavity, , Int. J. Therm. Sci., 43 (2004) 849-864.

[Ramachandran, 1971] G.N. Ramachandran and A.V. Lakshminarayanan, Three-dimensional reconstruction from radiographs and electron micrographs: Application of convolutions instead of Fourier transforms, Proc. Nat. Acad. Sci. USA, 68 (9) (1971) 2236-2240.

[Ranjan, 2005] Manoj Ranjan, Interferometric study of steady and unsteady convection in cylindrical and eccentric annuli, M.Tech. dissertation, Indian Institute of Technology, Kanpur, India, (2005).

[Rasenat, 1989] S. Rasenat, G. Hartung, B.L. Winkler and I. Rehberg, The shadowgraph method in convection experiments, Exp. Fluids, 7 (1989) 412-420.

[Rashkovich, 1990A] L.N. Rashkovich and B.Yu. Shekunov, Hydrodynamic effects in growth of ADP and KDP crystals in solution. I. Growth kinetics, Sov. Phys. Crystallogr., 35 (1) (1990) 96-99.

[Rashkovich, 1990B] L.N. Rashkovich and B.Yu. Shekunov, Morphology of growing vicinal surface; Prismatic faces of ADP and KDP crystals in solutions, J. Cryst. Growth, 100 (1990) 133-144.

[Schopf, 1996] W. Schopf, J.C. Patterson and A.M.H. Brooker, Evaluation of the shadowgraph method for the convective flow in a side heated cavity, Exp. Fluids, 21 (1996) 331-340.

[Settles, 2001] G.S. Settles, "Schlieren and Shadowgraph Techniques", (Springer, Berlin, 2001), 376 pp.

[Shagam, 1978] R.N. Shagam and J.C. Wyant, Optical frequency shifter for heterodyne interferometers using multiple rotating polarization retarders, Appl. Opt., 17 (1978) 3034-3035.

[Shiomi, 1980] Y. Shiomi, T. Kuroda and T. Ogawa, Thermal analysis of a growing crystal in an aqueous solution, J. Cryst. Growth, 50 (1980) 397-403.

[Shlichta, 1985] P.J. Shlichta, Crystal growth in a spaceflight environment: final report, Materials processing in space environment, Experiment # 770100, (September 1985), pp. 1-123, (Jet Propulsion Laboratory, Pasadena, CA 91109).

[Singh, 2009] Vishnu Singh, M.Tech. dissertation, Indian Institute of Technology, Kanpur, India (2009).

[Singh, 2007] S.K. Singh, P.K. Panigrahi and K. Muralidhar Effect of buoyancy on the wakes of circular and square cylinders - a schlieren-interferometric study, Experiments in Fluids, 43 (2007) 101-123.

[Smigielski, 1970] P. Smigielski and A. Hirth, Proc. 9th Internat. Congress on High-Speed Photography, W.G. Hyzer and W.G. Chase (Eds.), (SMPTE, New York, 1970), pp. 321-326.

[Solitro, 1989] F. Solitro, L. Gatti, F. Bedarida, G.A. Dall'Aglio and L. Michetti, Multidirectional holographic interferometer (MHOI) with fiber optics for study of crystal growth in microgravity, SPIE 1162 (1989) 62-65.

[Srivastava, 2004] A. Srivastava, K. Muralidhar and P.K. Panigrahi, Comparison of interferometry, schlieren and shadowgraph for visualizing convection around a KDP crystal, J. Cryst. Growth, 267 (2004) 348-361.

[Steel, 1983] W.H. Steel, "Interferometry", 2nd ed., (Cambridge University Press, Cambridge, 1983), 320 pp.

[Trolinger, 1991] J.D. Trolinger and R.B. Lal (Eds.), "Crystal Growth in Space and Related Optical Diagnostics", SPIE 1557 (1991) 1-296.

[Verga, 1997] A. Verga, P. Baglioni, O. Dupont, J.L. Dewandel, T. Beuselinck and J. Bouwen, Use of electronic speckle pattern interferometers for the analysis of convective states of liquids in weightlessness, Proc. SPIE Vol. 3172, Optical Technology in Fluid, Thermal, and Combustion Flow III (1997) 194-210.

[Verma, 2003] Sunil Verma, S.K. Sharma, K. Muralidhar and V.K. Wadhawan, Optical imaging techniques in crystal growth research, in: "Crystal Growth of Technologically Important Electronic Materials", K. Byrappa, H. Klapper, T. Ohachi & R. Fornari (Eds.), (Allied Publishers, Bangalore, 2003), pp. 616-619.

[Verma, 2005A] Sunil Verma, K. Muralidhar and V.K. Wadhawan, Convection during growth of KDP crystals: Flow visualization and modeling, Ferroelectrics, 323 (2005) 25-37.

[Verma, 2005B] Sunil Verma, K. Muralidhar and V.K. Wadhawan, Convection and concentration mapping during crystal growth from solution using Mach-Zehnder interferometry and computerized tomography, Proc. 3rd Asian Conf. Crystal Growth & Crystal Technology (CGCT-3), Oct. 16-19, 2005, Beijing, China.

[Verma, 2005C] Sunil Verma, A. Srivastava, V. Prabhakar, K. Muralidhar and V.K. Wadhawan, Simulation and experimental verification of solutal convection in the initial stages of crystal growth from an aqueous solution, Ind. J. Pure & Appl. Phys., 43 (2005) 24-33.

[Verma, 2006] Sunil Verma, K. Muralidhar and V.K. Wadhawan, Determination of concentration field around a growing crystal using shadowgraphic tomography (Chap. 14), In: "Computerized Tomography for Scientists and Engineers", P. Munshi (Ed.), (CRC Press, New York, 2006) 158-174

[Verma, 2007] Sunil Verma, Convection, concentration, and surface feature analysis during crystal growth from solution using shadowgraphy, interferometry and tomography, Ph.D. dissertation, Indian Institute of Technology, Kanpur, India (2007).

[Verma, 2008A] Sunil Verma and P.J. Shlichta, Imaging techniques for mapping of solution parameters, growth rate, and surface features during the growth of crystals from solution, Prog. Cryst. Growth & Charact. Materials, 54 (2008) 1-120

[Verma, 2008B] Sunil Verma and K. Muralidhar, Three-dimensional reconstruction of convective features during crystal growth from solution using computerized tomography, In: "CT2008: Tomography Confluence", P. Munshi (Ed.), American Institute of Physics CP 1050 (2008) 103-114

[Verma, 2009] Sunil Verma and K. Muralidhar, Convection, concentration, and surface features analysis during crystal growth from solution using optical diagnostics (Chap. 5), in: Recent Research Developments in Crystal Growth, Vol. 5 (2009) 141-314 (Transworld Research Network, India)

[Vest, 1979] C.M. Vest, "Holographic Interferometry", (John Wiley, New York, 1979), 465 pp.

[Vikram, 1990] C.S. Vikram, H.J. Caulfield, G.L. Workman, J.D. Trolinger, C.P. Wood, R.L. Clark, A.D. Kathman and R.M. Ruggiero, Two-color holographic concept (T-CHI), Final Tech. Rep., Contract No. NAS8-38078, NASA George C. Marshall Space Flight Centre (April 1990).

[Vikram, 1991] C.S. Vikram, W.K. Witherow and J.D. Trolinger, Refractive properties of TGS aqueous solution for two-color interferometry, SPIE 1557, "Crystal Growth in Space and Related Optical Diagnostics", J.D. Trolinger and R.B. Lal (Eds.), (1991) 197-201.

[Vikram, 1992A] C.S. Vikram and W.K. Witherow, Critical needs of fringe-order accuracies in two-color holographic interferometry, Exp. Mech., (March 1992) 74-77.

[Vikram, 1992B] C.S. Vikram, W.K. Witherow and J.D. Trolinger, Determination of refractive properties of fluids for dual-wavelength interferometry, Appl. Opt., 31 (34) (1992) 7249-7252.

[Witherow, 1987] W.K. Witherow, Reconstruction techniques of holograms from Spacelab-3, Appl. Opt., 26 (12) (1987) 2465-2473.

[Witherow, 1994] W.K. Witherow, J.R. Rogers, B.R. Facemire, S.D. Armstrong, J.D. Trolinger, D. Weber and C.S. Vikram, Methods to detect and measure gradients in fluids and materials processing, Proc. 6th International Symp. on Experimental Methods for Microgravity Materials Science, San Francisco (USA), Feb. 27- March 3, 1994, R.A. Schiffman and B. Andrews (Eds.), The Minerals, Metals and Materials Society, 33-37.

[Wyant, 1975] J.C. Wyant, Use of an AC heterodyne lateral shear interferometer with real-time wavefront correction systems, Appl. Opt., 14 (1975) 2622-26.

[Wyant, 1978] J.C. Wyant and R.N. Shagam, Use of electronic phase measurement techniques in optical testing, Proc. 11th Congr. of the International Commission for Optics, Madrid, 10-17 September 1978, J. Bescos, A. Hidalgo, L. Plaza and J. Santamaria (eds.) (Sociedad Espanola de Optica, Madrid) pp. 659.

[Wyant, 1982] J.C. Waynt, Interferometric optical metrology: Basic systems and principles, Laser Focus, (May 1982) 65-71.

[Wyant, 1985] J.C. Wyant and K. Creath, Laser Focus, (November 1985), pp. 118.

[Xiling, 1992] Yu Xiling and Yue Xuefeng, Holographic studies of diffusivities of KDP and DKDP in the solutions, Cryst. Res. Technol., 27 (1992) 825-830.

[Xiling, 1996] Yu Xiling, Sun Yi, Jiang Huizhu and Zhnag Shujun, Growth kinetics of the metastable tetragonal phase of potassium dideutrium phosphate (DKDP) crystals, J. Cryst. Growth, 166 (1996) 195-200.

[Yin, 2001] D. Yin, Y. Inatomi and K. Kuribayashi, Study of lysozyme crystal growth under a strong magnetic field using a Mach-Zehnder interferometer, J. Cryst. Growth, 226 (2001) 534-542.

[Yin, 2003] D.C. Yin, Y. Inatomi, N.I. Wakayama and W.D. Huang, Measurement of temperature and concentration dependences of refractive index of hen-egg-white lysozyme solution, Cryst. Res. Technol., 38 (9) (2003) 785-792.